

Refractive X-ray beam shaping

Zur Erlangung des akademischen Grades eines

DOKTORS DER INGENIEUR- WISSENSCHAFTEN (Dr.-Ing.)

von der KIT-Fakultät für Elektrotechnik und Informationstechnik des
Karlsruher Instituts für Technologie (KIT)
angenommene

DISSERTATION

von

Dipl.-Ing. Otto Thomas Markus

Tag der mündlichen Prüfung:	02. August 2022
Hauptreferent:	Prof. Dr. Ulrich Lemmer
Korreferent:	Prof. Dr. Volker Saile

Abstract

This work introduces new refractive illumination optics in the hard X-ray region and describes a method for overcoming fabrication limitations of X-ray depth lithography. In particular, the problem of high aspect ratio in X-ray prism lenses was addressed. The refractive X-ray optics are developed for the photon energy range 8-100 keV. In the following, we report the development of a principal new focusing optics with large aperture, an illumination condenser for full-field X-ray microscopy and a so-called beam shaping optics to overcome the limitation of the field of view at 3rd and 4th generation synchrotron sources.

To reduce the absorption of X-rays in the material of the optical systems, the approach of X-ray prism lenses was pursued. Here, the optics consist of rows of micro prisms with an edge length of about 20 μm , which deflect the incident rays. This improves the ratio of the refractive power of the optics to the volume of the absorbing lens material. The mechanical stability of the fragile, very tall micro prisms is achieved by exposing thin, stabilizing support planes.

In order to achieve focal sizes smaller than the prism edge lengths, double-parabolic biconcave micro-lenses were added to the prism rows. A similar arrangement with biconvex micro-lenses was used to achieve beam expansion while simultaneously homogenizing the illumination of the image field of a full-field X-ray microscope. Beam shaping optics consisting of kinoform Fresnel lens elements were developed for vertical beam expansion at high-brilliance synchrotron sources.

In all cases, the theory is based on geometrical optics and ray tracing simulations. The optics were produced via deep X-ray lithography using the synchrotron radiation source at KIT at the LIGA I and II beamlines. The lens material is the negative resist mr-X, an epoxy resin-based polymer of type

SU-8. The lenses were characterized at PETRA III, DESY in Hamburg and at ESRF in Grenoble.

Kurzfassung

Im Rahmen dieser Arbeit wurden neue refraktive Beleuchtungsoptiken im harten Röntgenbereich und eine Methode zur Überwindung der Technischen Grenzen von der Röntgentiefenlithografie erarbeitet. Insbesondere wurde das Problem des hohen Aspektverhältnisses in Röntgenprismenlinsen untersucht. Die refraktiven Röntgenoptiken finden ihren Einsatz im Photonenenergiebereich von 8-100 keV. Drei neuartige Röntgenoptiken wurden entwickelt: eine speziell neue Fokussieroptik mit großer Apertur, ein Beleuchtungskondensator für die Vollfeldröntgenmikroskopie und eine Strahlformoptik zur Überwindung der Einschränkung des Bildfeldes bei Synchrotronquellen der 3. und 4. Generation.

Zur Reduzierung der Absorption der Röntgenstrahlung im Material der Optiken wurde der Ansatz der Röntgenprismenlinsen verfolgt. Dabei besteht die Optik aus Reihen von Mikroprismen mit etwa 20 μm Kantenlänge, welche die einfallende Strahlung umlenken. So wird das Verhältnis von Brechkraft der Optik zum Volumen des absorbierenden Linsenmaterials verbessert. Die mechanische Stabilität der fragilen Mikroprismen wird durch eine zusätzliche Belichtung für dünne, stabilisierende Stützebenen erreicht.

Um Fokusgrößen kleiner als die Prismenkantenlängen erreichen zu können, wurden den Prismenreihen doppelparabolisch geformte bikonkave Mikrolinsen hinzugefügt. Mit einer ähnlichen Anordnung mit bikonvexen Mikrolinsen wurde eine Strahlaufweitung bei gleichzeitiger Homogenisierung der Ausleuchtung des Bildfeldes eines Vollfeldröntgenmikroskops erreicht. Eine Strahlformungsoptik aus kinoformen Fresnel-Linsenelementen wurde zur vertikalen Strahlaufweitung an hochbrillanten Synchrotronquellen entwickelt.

Die Theorie basiert in allen Fällen auf geometrischer Optik und Strahlverfolgungssimulationen. Die Optiken wurden mit Hilfe der Synchrotronstrahlungsquelle am KIT an den Strahlrohren LIGA I und II röntgentiefenlithografisch hergestellt. Das Linsenmaterial ist der Negativresist mr-X, ein Polymer

vom Typ SU-8 auf Epoxidharzbasis. Die Charakterisierung der Linsen erfolgte an PETRA III, DESY in Hamburg und an ESRF in Grenoble.

Acknowledgement

Special thanks go to my doctoral advisor Prof. Dr. Ulrich Lemmer for taking over the duty of being the referee of this thesis. I thank for the support for this work as well as for his advises. I would like to thank Prof. Dr. Volker Saile for his interest, helpful comments and suggestions and for being a referee.

The biggest thanks go to my supervisor Dr. Arndt Last for the excellent, constructive, motivating and endless support all along the years of the practical work and especially along writing.

Furthermore, thanks to Dr. Jürgen Mohr for the great support of the work as well as the leadership of the X-ray group of IMT, additionally, for his work in the correction process and new perspectives in publications and in this dissertation.

I thank the Karlsruhe Nano Micro Facility (KNMF) for funding and fabricating the essential lithographic structures of my work. For my scholarship and for the opportunity to attend to numerous interesting lectures, I thank the Karlsruhe School of Optics and Photonics (KSOP), especially Stefanie Peer for administrative help. At this point, I would like to thank Dr. Martin Lauer for his support and collaboration as my PhD mentor in KSOP.

Likewise, I thank Dr. Imke Greving and Dr. Malte Storm for their support during my beam times at P05 at DESY. I thank Dr. Angelica Cecilia and the whole team of Topo-Tomo at KARA.

Thanks also to all the staff of KIT/IMT. Andreas Bacher for his role in taking good care of layout and electron beam lithography related tasks. Martin Börner especially for the assistance with irradiations of the lenses at the lithography beamlines at KARA. Danays Kunka, Pascal Meyer and Klaus Bade for sharing their years of experience. I thank many other staff members of the institute for their versatile and competent contributions to my work.

Especially Heike Fornasier and Uwe Köhler for their support in the clean room, Giuseppe Papagno for the precise dicing works on my lens plates, Alexandra Moritz and the workshop team for the supporting activities, Ulrich Klein for the IT support, Nina Giraud for her help whenever I had issues with ordering something via SAP. Furthermore, I would like to thank my fellow PhD student colleges, especially Frieder, Jan, Tobias, Sebastian, Vitor, Abrar, Alex, Talgat, Margarita and Andrey, both for their professional and private contribution in our team and for making the days spent with work a lot more fun.

A very big thank you goes to Dr. Joachim Schulz and the whole microworks team. Without their support, most probably this work would still sit on my desk, waiting to be done.

Additionally, I thank my parents for planting the seeds of interest in me so deeply that I was able to carry out this task.

On the end of this far from complete list, I would like to express my deepest gratitude to my wife, Elisa. This work never would have been completed without her gentle and never resting but still necessary encouragement. I thank her for her endless patience and motivation in overwhelming times, for her help and openness for professional discussion and especially for the brightness, joy and challenges she brings in my life. In short: motivating me to become a better person.

Bad Herrenalb, June 2022

Otto Markus

Table of Content

Abstract	i
Kurzfassung	iii
Acknowledgement	v
Table of Content	vii
1 Introduction and motivation	1
2 Background	5
2.1 X-ray sources	5
2.2 X-rays interacting with matter	10
2.3 Overview X-ray optics	12
2.4 Refractive X-ray optics	15
2.4.1 Compound refractive lenses	15
2.4.2 Fresnel or kinoform lenses	16
2.4.3 X-ray prism lenses (XPLs)	17
3 Layout and fabrication of refractive X-ray optics	19
3.1 Tools for optics validation via raytracing	19
3.2 Deep X-ray lithography	19
3.2.1 Intermediate mask production	20
3.2.2 Working mask production	22
3.2.3 X-ray lens production	23
3.3 Measurement of the refractive index for the lens materials	25
3.4 Fabrication limitations	28
3.5 Reinforcement of XPLs	29
4 Focusing with X-ray prism lenses	39
4.1 Aim and main challenges	40
4.2 New concept	41

4.3	Realization	48
4.4	Results	51
4.5	Summary focusing prism lenses	54
5	Condenser optics for full field microscopy	57
5.1	Aim and main challenges	58
5.2	New concept	61
5.3	Realization	63
5.4	Results	66
5.5	Summary prism condensers	69
6	Optimizing synchrotron source illumination for full field imaging ..	71
6.1	Aim and main challenges	71
6.2	Design considerations	72
6.3	Realization	78
6.4	Simulation and experimental results	80
6.5	Summary beam widening lenses	86
7	Conclusion and outlook	89
	Appendix	93
A	Lens layout parameters	95
B	Calculation software	101
C	List of own publications	105
	References	107

1 Introduction and motivation

In many scientific fields, X-rays are a widely used and important analytical tool. Due to their high penetration depth, they successfully can be used to examine the composition and structure of most materials. This opens up a wide range of applications for scientific, technical and medical applications.

In addition to the penetration characteristics, the short X-ray wavelength enables higher spatial resolution than optics in the visible regime, due to the much lower diffraction limit. Thus, higher resolution can be achieved even with a simple shadow projection of absorbing samples, which to date is used by most X-ray optical imaging techniques. Even more advantageous are focused X-rays in this regard, whether it is to increase the resolution of an imaging system, or to reduce the time required for an experiment by increasing the photon density at sample position. The X-ray beam can be shaped with the use of various techniques. Focusing for example, can be realized via reflection from curved X-ray mirrors, diffraction from zone plates or refraction from refractive X-ray lenses. At photon energies above about 15 keV, the use of refractive lenses is advantageous over zone plates due to their higher efficiency.

In this work, new illumination schemes of refractive X-ray lenses were developed especially for the hard X-ray regime. They offer not only to overcome current limitations in focusing optics but also in homogenous illumination applications, in full field X-ray microscopy as well as in the illuminated field of view (FoV) specifically in the case of high brilliance synchrotron sources. This is becoming even more relevant with time, as synchrotron development tends to increase brilliance, which mostly means at the same time sacrificing FoV at sample position.

The need for flexible illumination optics with high efficiency, also offering homogeneous illumination and possibly enlarge the FoV is easily under-

standable. With optimal illumination the experiments and investigations can be carried out faster and in most of the cases the quality of the results improves as well. In contrast to imaging optics, the most important criterion of illumination is the achievable maximum photon efficiency. This has two aspects: the first is maximising effective entrance aperture for collecting as many photons as possible. The second is to maximise the transmission of the optical system.

With these boundary conditions, concepts based on Fresnel- and X-ray Prism Lenses (XPLs) are most promising. The advantages of these lenses compared to the normally used Compound Refractive Lenses (CRLs) from the aspect of illumination are the larger effective aperture and the high flexibility of design. Each small beamlet entering a prism row can be calculated separately instead of calculating the whole beam cross section at once. Up to now, the fabrication capabilities were the limiting factor of these lenses but in this work, a technique will be shown to overcome it.

Three different X-ray optics have been developed and characterized in this work: a large aperture focusing optics, a condenser optics for full field microscopy and a so-called beam shaping optics to widen the nearly parallel synchrotron beam for providing an optimally tailored illumination of samples.

To conduct this work, it was first necessary to understand the physical background of X-ray optics and the current state of existing refractive X-ray optics (chapter 2). The X-ray optics are fabricated by deep X-ray lithography, which poses some technical limitations on the structural size of the optical elements. This will be discussed in chapter 3. The developments and achievements of the three different elements will be described in three different chapters. First, the need and challenges will be analysed and specifications will be derived. Following, the proposed solution and design will be theoretically analysed, underlined by simulation. The realized modifications in the fabrication process will be presented in the third sub-chapter, whereas in the fourth sub-chapter the experimental results will be described. Each chapter will finish with a conclusion for the specific lens type. In chapter 7 of

this thesis, the results will be summarized, an overall conclusion is given and advice for further work to improve the optics are provided.

2 Background

X-rays are electromagnetic radiation in the wavelength range between ultra-violet and gamma radiation. The spectrum of the wavelength λ ranges from about 10 nm to 1 pm. In the field of X-ray optics, the photon energy E/keV is used to specify X-rays. With Planck's quantum of action h , the velocity of light c_0 and the wavelength λ the photon energy is calculated by

$$E = \frac{c_0 h}{\lambda}. \quad (2.1)$$

The typical range of X-rays used for X-ray optics in this work is from $E = 8 \text{ keV}$ to 100 keV . This chapter describes today's X-ray sources first, then interaction of X-rays with materials and the optical elements used to manipulate X-ray beams.

2.1 X-ray sources

In this work, optics for using at synchrotron sources have been developed. So some properties of these sources will be discussed. To characterize optical properties of sources, performance, brilliance, photon flux and spectrum will be used as a measure [1], [2].

The brilliance is the photon flux within a specific spectral bandwidth BW, source area, per second and in a solid angle [1].

$$\text{brilliance} = \frac{\text{photons}}{\text{second} \cdot \text{mrad}^2 \cdot \text{mm}^2 \cdot 0.1\% \text{BW}} \quad (2.2)$$

Synchrotron accelerator based sources are the result of a long history in the development of X-ray sources and have the highest brilliance of all the X-ray sources used in research (Figure 2-1).

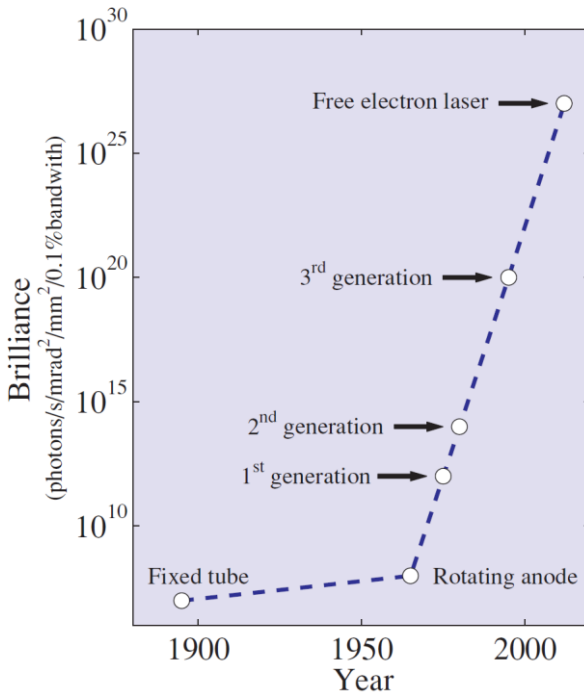


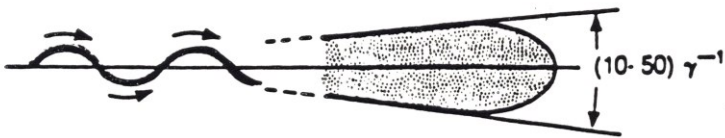
Figure 2-1: Comparison of sources from the aspect of average brilliance. Worth to notice that the peak brilliance of free electron lasers exceeds the average brilliance by multiple orders of magnitude due to the extremely short pulse length of order 100 fs [1]

Synchrotron sources

Synchrotron radiation is emitted by a particle accelerator in which an electron or positron beam is travelling in a closed loop at relativistic speed. To keep the trajectory of the particles, a magnetic field perpendicular to the beam velocity vector is applied. The particles exposed to centripetal forces emit photons tangential to their flight direction. Figure 2-2 shows principle sketches of a bending magnet, keeping the beam in a closed loop, and insertion devices such as wigglers or undulators [3], [4].

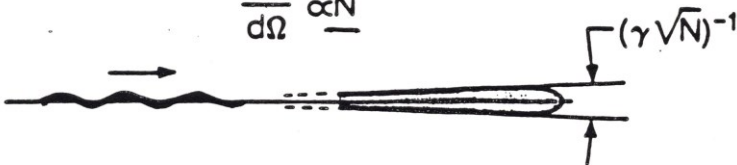


Bending Magnet — A "Sweeping Searchlight"



Wiggler — Incoherent Superposition

$$\frac{dP}{d\Omega} \propto N$$



Undulator—Coherent Interference

$$\begin{aligned} \frac{dP}{d\Omega} &\propto N^2 \\ \Omega &\propto \frac{1}{N} \\ P &\propto N \end{aligned}$$

Figure 2-2: Principle sketch of a bending magnet, keeping the beam in a closed loop, and different insertion devices in a synchrotron source; γ is the photon energy E over the invariant mass of the accelerated particle m_0 multiplied by speed of light c squared, N the number of magnetic periods (~ 100) [4].

Synchrotron sources are many orders of magnitude more brilliant than conventional X-ray tubes and the light emission is pulsed because the particles

travel in bunches in the storage ring. The light is highly polarized and has a small angular divergence at least in one dimension. A narrow wavelength range can be filtered further using a monochromator.

Bending magnets

Necessary components of the storage ring are bending magnets, as they are responsible for the particles to stay on a closed trajectory. Photon emission, generated by a bending magnet has vertically a low angular divergence but horizontally is only limited by the beamline construction parameters (see Figure 2-2 top part). The radiation is linearly polarized, in the plane of the orbit. Out of this plane, the polarization is elliptical.

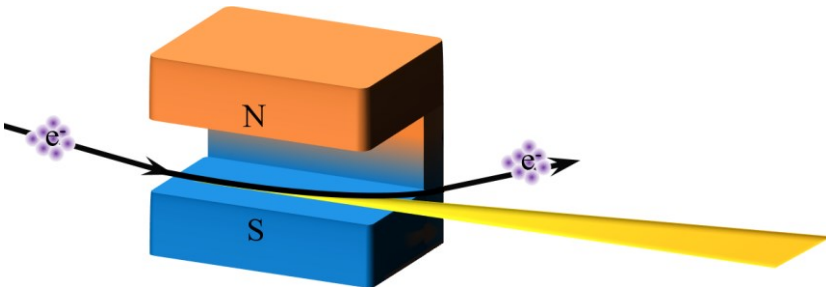


Figure 2-3: Radiation from a bending magnet, showing the interaction between the particle bunch e^- and the magnetic field, where N indicates the north, as S the south pole. The emitted X-ray beam is visualized in yellow.

Wiggler

In wigglers the intensity is increased by lining up several of small bending magnets (dipoles) along the electrons trajectory. These dipoles are arranged with an alternating magnetic polarity. So the electrons flying through a periodic sinusoidal magnetic field varying like:

$$B(z) = B_0 \cdot \cos\left(\frac{2\pi z}{\lambda_u}\right). \quad (2.3)$$

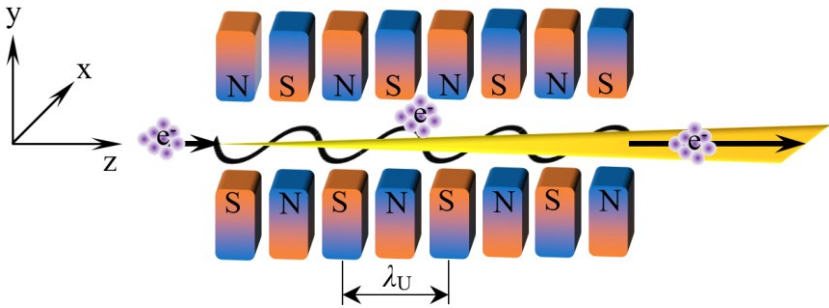


Figure 2-4: Periodic structures of dipoles at a wiggler/undulator source; λ_u is the magnetic period, N is the north and S is the south pole

Where z is the length of the periodically alternating field, B_0 is the amplitude of the flux density and λ_u is the magnetic period. The electron trajectory is in a horizontal plane and can be described by a sinusoidal function.

The deflection – or undulator – parameter K is used to characterize the electron motion:

$$K = \frac{eB\lambda_u}{2\pi m_e c}. \quad (2.4)$$

Where e is the electron charge, B is the magnetic field, λ_u is the magnetic period m_e is the electron rest mass, and c is the speed of light.

If $K \gg 1$ the oscillation amplitude is bigger and the radiation contributions from each field period sum up independently, leading to a broad energy spectrum. Under this working principle, the device is called a wiggler.

Undulator

For $K \ll 1$ the oscillation amplitude of the motion is small and the radiation displays interference patterns, which lead to narrow energy bands. In this case, the insertion device is called an undulator. The narrow bandwidth can be advantageous when requiring higher intensity at certain photon energies

and can be further narrowed down by monochromators. In contrast to Wigglers, the photons emitted from the individual poles overlap coherently and cause constructive interference [5].

Thus, the radiation is more intense and better collimated than in the case of wigglers. Undulators typically have a brilliance in the range of 10^{20} - 10^{23} photons/s/mm²/mrad²/0.1%BW, more than five orders of magnitude higher than bending magnets [1]. The low angular divergence of modern synchrotron insertion sources provide highly collimated radiation in both horizontal and vertical direction. Nevertheless, in the case of full-field imaging, despite the advantage of higher brilliance this limits the field of view, thus the maximum sample size.

2.2 X-rays interacting with matter

When X-rays pass through matter, the electromagnetic radiation interacts with the matter in various ways. The X-rays attenuated by absorption and the photons refracted, diffracted and scattered. After leaving the medium, the phase has shifted with respect to a wave that has not passed through matter. Furthermore, the intensity I of the wave is attenuated. These phenomena can be described with the complex refractive index n^* , which depends on the scattering factors f' and f'' (see equation (2.9) and (2.10)) of the atoms present in the material [6]:

$$n^* = 1 - \delta + i\beta . \tag{2.5}$$

The variables δ and β are real numbers and positive for X-rays. Here, δ denotes the refractive index decrement and β the extinction coefficient. Snell's law describes the refraction at surfaces, where the real part of the refractive index $n = \Re(n^*) = 1 - \delta$ is used for non-absorbing materials:

$$n_i \sin \theta_i = n_t \sin \theta_t . \tag{2.6}$$

The angle θ_i denotes the angle between the incident beam and the surface normal and θ_t the angle between the transmitted beam and the surface normal. The linear attenuation coefficient for absorption

$$\mu = \frac{4\pi\beta}{\lambda} \quad (2.7)$$

is determined with the imaginary part of the refractive index $\beta = \Im(n^*)$ and is used to describe the absorption in Lambert-Beer's law:

$$I(z) = I_0 e^{-\mu z} \quad (2.8)$$

The change in intensity I by absorption is described as a function of the distance z travelled in the material. The variables δ and β result from the scattering factors f' and f'' [7] with

$$\delta = \frac{\lambda^2}{2\pi} r_0 N_A \frac{\rho}{A} (Z + f') \quad (2.9)$$

and

$$\beta = \frac{\lambda^2}{2\pi} r_0 N_A \frac{\rho}{A} f'' \quad (2.10)$$

where r_0 is the classical electron radius, N_A is the Avogadro constant and ρ is the density, A is the atomic mass and Z is the atomic number.

For the short wavelength of X-rays (1 pm to 10 nm), the index of refraction of all matter is slightly below unity. Both the refractive index decrement and the extinction coefficient are very small, in the photon energy range where refractive lenses are used, $10^{-7} < \delta < 10^{-5}$ and β even two magnitudes less. Good candidates for a lens material have a high δ/β ratio, i.e. a high refractive power at low absorption. Low atomic Z -number materials are good candidates for refractive optics, such as lithium [8], [9], beryllium [10], carbon (diamond) [11], aluminium [10], silicon [11], [12] and nickel [13] and the polymer SU-8 [14], [15]. Figure 2-5 shows the correlation between photon energy, atomic mass and δ/β ratio for some low Z -number materials.

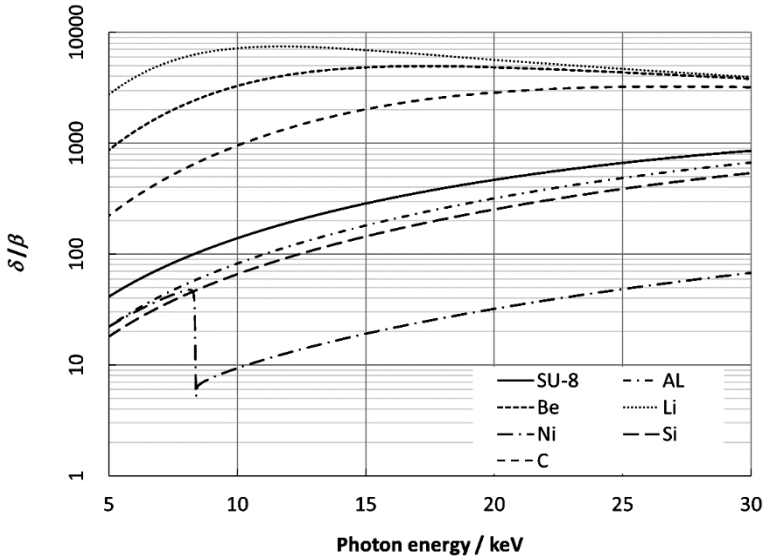


Figure 2-5: Relation between δ/β ratio and lens material with respect to photon energy from 5 to 30 keV [16]

Based only on theoretical requirements, lithium seems to be a perfect candidate. However, alkali metals are extremely reagent and unstable in normal environment, so they are not applicable for X-ray lenses in practice. Beryllium is theoretically the second best choice and is used as material for compound refractive lenses, but it is carcinogen, requires extreme caution in manufacturing and properly made housing. Glassy carbon and diamond are also used as lens material, but are brittle and tricky to manufacture. At KIT/IMT refractive X-ray optics an epoxy-based polymer, a certain type of SU-8 photoresist is used to lithographically manufacture X-ray lenses.

2.3 Overview X-ray optics

The characteristics of the raw beam leaving the source normally limit the possible applications. Numerous different X-ray optics have been developed throughout the years to shape or focus the beam. Their purpose can be sum-

marized in short as influencing or redefining the ray distribution and/or spectrum of the incident beam, tailored exactly in a well-defined way.

Based on the physical principle these optics rely the most on, we can classify them accordingly. In the following, I will list the state-of-the-art optics.

Absorption optics, exploiting the energy related and finite penetration depth of X-rays, can be windows, apertures, resolution test structures, pin-holes, slits, filters, coded masks and absorption gratings.

X-rays can as well be reflected by total external reflection (TER) at surfaces with small incident angles. Reflective X-ray optics can be TER- or crystal-mirrors, Kirkpatrick-Baez mirrors, Wolter mirrors, Montel mirrors, rolled mirror optics, micro channel optics, lobster eye optics and mono- or polycapillary optics.

X-rays, as every electro-magnetic wave, are diffracted. The grating constant has to be in the nanometre range to achieve large diffraction angles. Fabricated objects – limited by the possibilities given today – even with a much larger grating constant can influence the direction of the beam enough, that it is sufficient for X-ray optical purposes. Some types of diffraction X-ray optics are: zone plates, Bragg-mirrors, multilayer mirrors, multilayer Laue lenses and phase gratings.

Finally, X-rays are refracted at the physical interface between different materials. X-ray optics, which rely mostly on this effect, are called refractive X-ray optics and will be discussed in the following chapters. Generally, these are compound refractive lenses, mosaic lenses, alligator lenses, rolled- and standing prism lenses.

Figure 2-6 shows a rough summary of state-of-the-art X-ray optics.

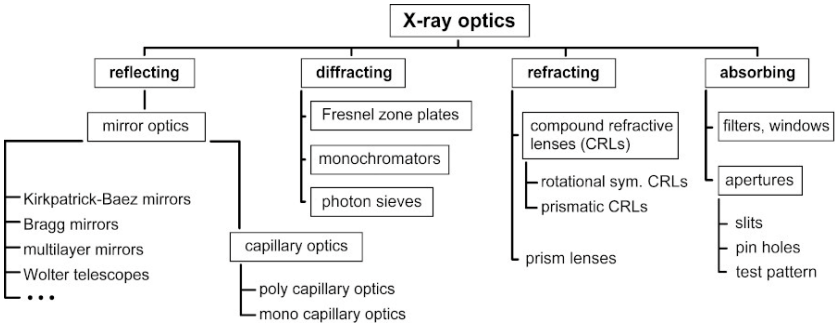


Figure 2-6: Overview of X-ray optics based on their physical principle [17]

In the following, I will present the main characteristics of X-ray optics as a comparison, in the form of a table.

Table 2-1: Comparison of X-ray optics regarding their main characteristics photon energy range, working distance, minimal focal spot diameter, application in imaging or illumination and achromatic behaviour [17]

physical principle	optics type	photon energy range [keV]	working distance [m]	min. focal spot diameter [μm]	imaging or illumination	achromatic behaviour
reflection	mirror optics	0 - 20	>0.1	0.03	imaging	yes
	multi layer / crystal mirror optics	0 - 100	>0.1	0.05	imaging	no
	polycapillary optics	0 - 20	0.002 - 0.2	1	illumination	yes
	mono capillary optics	0 - 20	0 - 0.2	<1	imaging	yes
diffraction	zone plates	0 - 20	0.001 - 0.1	0.015	imaging	no
refraction	compound refractive lenses	5 - 500	>0	0.1	imaging	no
absorption	coded mask telescopes	all	-	(10)	imaging	yes

2.4 Refractive X-ray optics

2.4.1 Compound refractive lenses

As it has been shown in chapter 2.2, the real part of the refractive index is slightly below unity. This results in a (bi)concave parabolic geometry of the refracting surfaces of a converging X-ray lens. As the refractive power of one single lens element is extremely small, an X-ray lens normally consists of multiple, sometimes hundreds of lens elements aligned in a straight row. Such an X-ray lens is called compound refractive lens (CRL). As shown in Figure 2-7, where f_a is the focal length of one single element, whilst f_b is the focal length of a lens made of N identical lens elements.

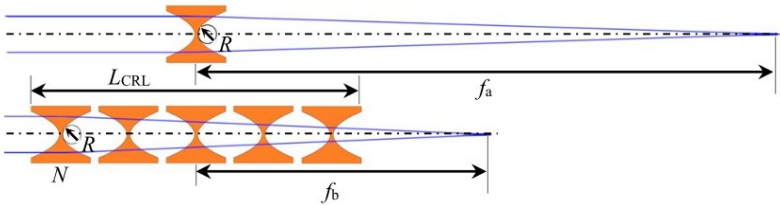


Figure 2-7: The difference between a focusing X-ray lens built up of one element (above) and multiple elements (below) with f_a and f_b the focal length, R the radius in the apex of the parabolas, L_{CRL} the length of the compound refractive lens and N the number of lens elements [18]

An important parameter of a CRL is its focal length. For a “thin lens”, meaning that its physical length along the optical axis is negligible compared to its focal length, the focal length is computed as

$$f_{thin} = \frac{R}{2\delta N} \quad (2.11)$$

where f_{thin} is the focal length, R is the radius in the apex of the parabolas, δ is the refractive index decrement and N is the number of lens elements [19]. In case of a “thick lens” with a physical length not negligible compared to the focal length, the length of the lens has to be included [20]:

$$f_{thick} = \frac{R}{2\delta N} + \frac{L_{CRL}}{6} \quad (2.12)$$

where L_{CRL} is the length of the lens, as shown in Figure 2-7.

The focal length can be reduced by reducing the radii of curvature of the refracting surfaces, as far as this is technically feasible. As a focusing lens has a biconcave shape, this means that the rays passing the outermost areas are highly absorbed, limiting the practically usable aperture. A measure of the useable aperture can be the distance from the optical axis where for rays parallel to the optical axis the transmittance of the lens drops below $1/e^2$ of the transmittance on the optical axis [6].

2.4.2 Fresnel or kinoform lenses

To overcome the problem of absorption limiting the effective aperture, an old technique was repurposed. Fresnel lenses [21] have been developed to reduce the mass of optical elements with large aperture. In the case of X-ray optics, the same technique helps to reduce the amount of lens material only contributing to absorption and not increasing the refractive power. The effective aperture of a CRL is limited to some hundreds of micro metres. This limitation is due to the amount of material in the bulk of the lens. The straightforward idea is, to remove the crosshatched area of a parabolic CRL in Figure 2-8. In case of coherent radiation, the length of the removed block in the direction of the optical axis has to be an integer multiple of the wavelength to achieve maximum intensity in the focus.

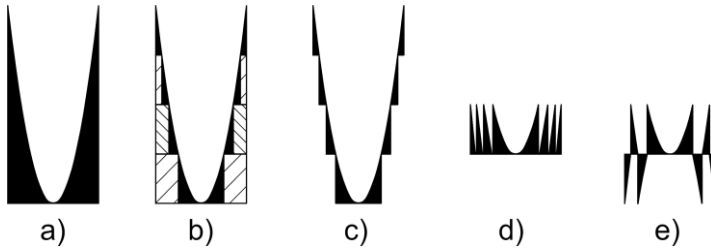


Figure 2-8: The composition of a kinoform or Fresnel-lens as a projection of high aspect ratio structures. a) parabolic profile, b) and c) material removed, d) shifting the optically relevant parts to form a compact design, e) flipping every second element, to get a geometry more easily accessible during manufacturing [22]

2.4.3 X-ray prism lenses (XPLs)

Limited by constraints in fabrication and aiming for even higher transmission, a new type of lenses has evolved from the kinoform lenses. Figure 2-9 a) shows a Fresnel lens, and its outermost element in Figure 2-9 b). As infinitely sharp corners only exist in theory, the rounding of the corners shrinks more and more the effective aperture. Furthermore, introducing the term “aspect ratio” that is defined as the height of the structure divided by the smallest edge length or diameter of its cross section. Further limitation is, as the thinner the elements cross-section gets, the more difficult to achieve desirable aspect ratios. Figure 2-9 b) and c) are having identical refractive power; still the prisms are more easily fabricated. Prisms with equilateral triangular cross-section are the best choice with respect to mechanical stability. The whole lens can be substituted with independent rows of prisms, offering similar focusing effect. Every single prism row will only redirect a beamlet equally high to the effective height of the prism cross section. Consequently, prism lenses are not imaging optics, but illumination optics. To get a point focus prism lens, two half-lenses are crossed, rotated by 90° around the optical axis. The height of the line focusing prism half-lenses has to be equal to the aperture width of the point focus prism lens (see also Figure 4-3).

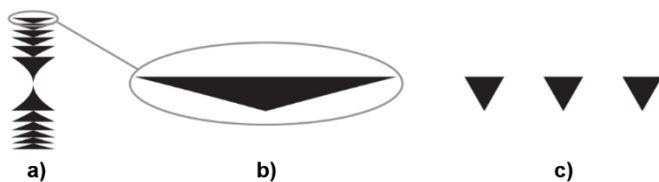


Figure 2-9: The evolution of prism lenses shown as a projection of high aspect ratio structures. a) Kinoform or Fresnel lens, b) Structure with extremely acute angle c) prisms, providing similar refractive power as b) [22]

3 Layout and fabrication of refractive X-ray optics

3.1 Tools for optics validation via raytracing

For designing the optical components, we rely on geometrical optics. The optical components considered in the following are built up from triangular prisms, convex and concave CRLs.

To design all of my optical components I used self-developed code written in MATLAB environment. See an overview of this software as flow charts in appendix B. The validation of the designed optical components involves raytracing simulation – explicitly using MATLAB, Zemax OpticStudio, and Microsoft Excel as software environment – of the models and practical experiments, in our case at synchrotron sources. As far as the simulation goes, it is crucial to have reliable source data, including not only the actual synchrotron source, but also optical elements interacting with the beam in front of the optics in question.

3.2 Deep X-ray lithography

The presented optics have been produced via deep X-ray lithography [23], [24], at the Accelerator Test Facility and Synchrotron Radiation Source at KIT (referred to as KARA in the following).

At IMT – the birth place of the X-ray LIGA (**L**ithographie, **G**alvanoformung, **A**bformung) process [25], [26] that is summarised in Figure 3-1 – as lens material an epoxy based negative tone photosensitive resist [27] has been chosen, a sub-type of SU-8 [28], namely mr-X-50 from *micro resist technology GmbH*, Berlin. Throughout the processing standard, 525 μm thick silicon

wafer served as substrates. Opposing a common misconception, mr-X-50 has proven having long-term radiation stability. Even at a level of 2 MJ/cm^3 dose deposition [29], these lenses serve with convincingly long lifetime.

As the first step of the practical fabrication, the designed layout has to be transferred onto an intermediate mask also known as low contrast mask. Low contrast in this case means enough absorption and sufficient contrast for the exposure of a 60-100 μm thick resist layer using 2.2-3.3 keV photon energy.

3.2.1 Intermediate mask production

The intermediate mask is normally made on a silicon carrier covered with a thin graphite layer, that acts as a barrier below the 2.3 μm thick titanium membrane, with a specially oxidised surface, serving for better adhesion of the resist. The photoresist in the case of the low contrast mask is *PMMA 950K A11* in the nominal thickness of 3 μm . The desired layout is written by an electron-beam writer into the resist layer, with precisely adopted parameters to every single layout, depending on the structure size and shapes. As PMMA is a positive tone resist there is no need of post exposure bake, the sample can be – and should be – developed as soon as possible, avoiding further degradation of the structures.

After being developed, dried and inspected, electroplating is the next step. The mask is plated with gold – acting later as X-ray absorber – because gold has a fairly high density and atomic number making it a good choice. The electroplated layer thickness has to be more than 1.8 μm thick at every position on the mask.

After the successful plating and stripping of the resist, the two most critical steps are ahead. First, an invar mask-frame has to be glued onto the surface of the titanium membrane. After this point the whole mask has to be lifted off the carrier substrate. The low adhesion graphite barrier – mentioned in the beginning – allows to lift-off the titanium membrane. As last step of the processing, an inspection is done at a scanning electron microscope. If the mask

is concluded as successfully made, the working mask can be made in the following.

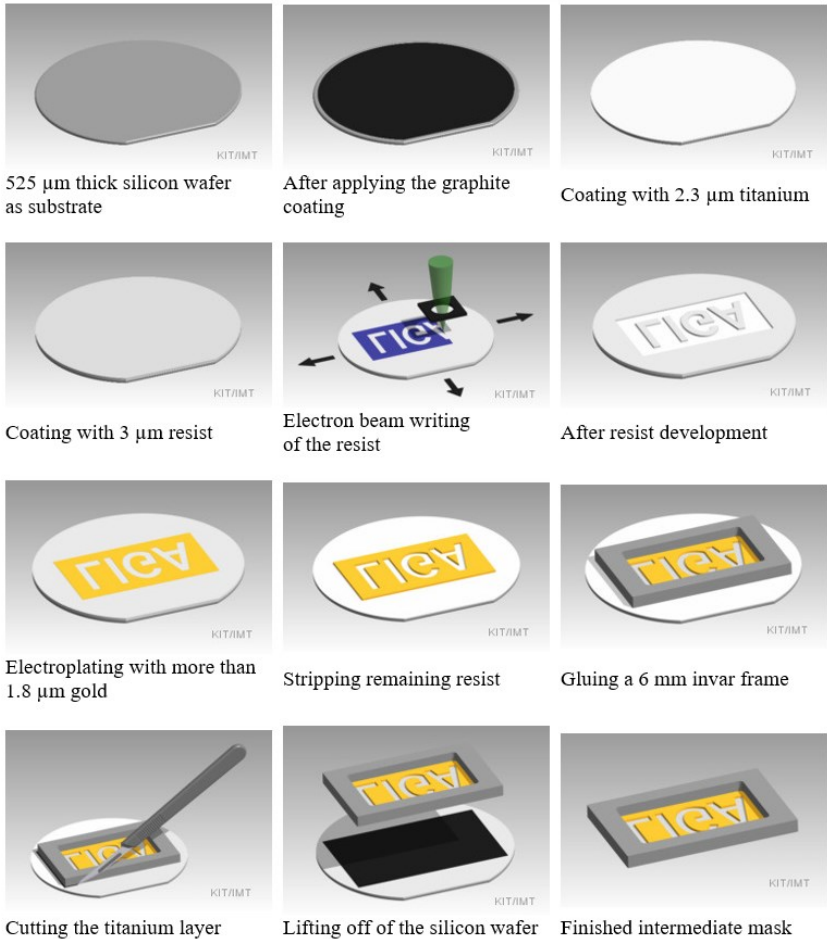


Figure 3-1: Intermediate mask fabrication step-by-step [17]

3.2.2 Working mask production

The high contrast mask is expected to provide sufficient contrast for an X-ray lithographic exposure into a few millimetres of resist thickness. As the working masks at IMT are used up to 12.4 keV of photon energy, the absorber thickness is required to be more than 24 μm . As this thickness cannot be written directly with an electron-beam writer, the intermediate mask is an unavoidable step in the production.

Depending on the requirements, it is possible to change the tone at this point of the photoresist. If the end product – in our case the lenses themselves – are expected to be an inverted copy of the intermediate mask, then for the working mask a negative resist has to be chosen. For the example shown here negative photoresist is chosen for the working mask production.

The working masks are produced on a 6 mm thick invar steel blank, containing on the front side the titanium layer that is coated with photoresist. The backside is machined, leaving a 2 mm thick material layer below the mask area, later to be etched away.

Similarly to the intermediate mask production, a 2.3 μm thick titanium coating will act as conductive barrier for the electroplating step. After coating the substrate with the necessary 60 μm of mr-X, a step of soft bake has to be carried out to reduce the solvent content of the resist to an ideal level for further processing. After some days of rest, the exposure can take place at the LIGA 1 beamline at the synchrotron source KARA. This bending magnet source, combined with a chromium mirror has a peak intensity at 2.5 keV and can be used for patterning photoresist up to 150 μm thickness. After exposure, the photoresist is not yet cross-linked. To initiate the cross linking process, the exposure is followed by a post exposure bake step (PEB). After the PEB, development can take place in an organic developer bath. After drying and inspection, electroplating has to be carried out to get the prescribed gold thickness of more than 24 μm . After successful coating, the back of the invar substrate must be etched free to expose the titanium membrane that supports

the mask absorbers. The membrane is held at the edges by the invar steel frame.

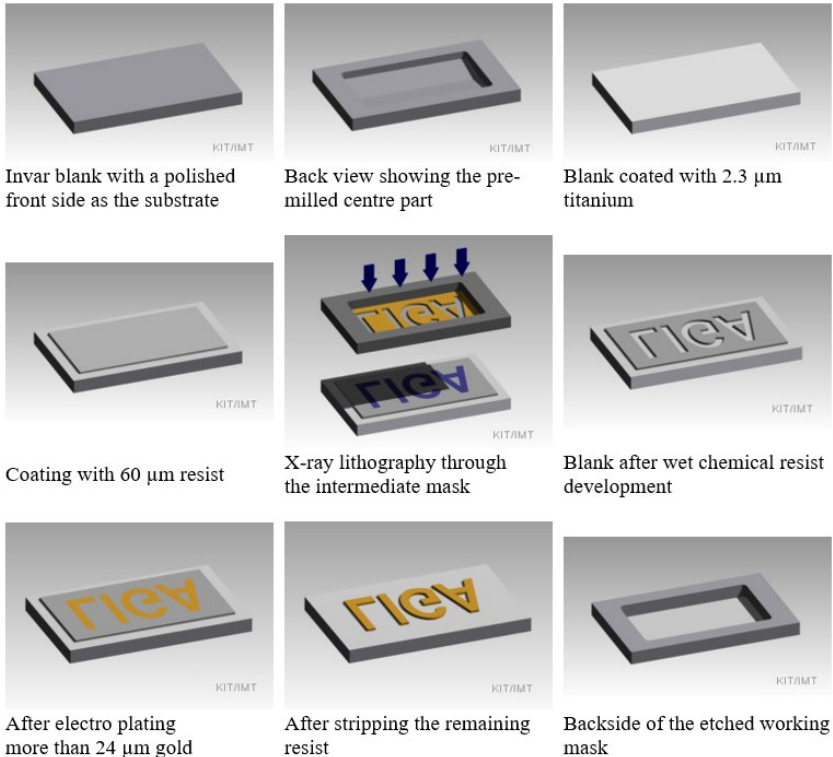


Figure 3-2: Working mask fabrication step-by-step [17]

3.2.3 X-ray lens production

The production of X-ray lenses by X-ray deep lithography follows the mask production in many steps.

The base resist material for the lenses is arriving in the form of coated silicon substrates to our institute. The standard 4", 525 μm silicon wafers used are

coated with 400, 800 or 2000 μm mr-X resist. These substrates can be used out-of-the-box for production.

The standard size of layout area is 20 mm x 60 mm for lens production. After proper inspection, the substrates are being mounted in the X-ray scanner at the beamline LITHO 2 at the synchrotron source KARA. LITHO 2 has a fairly wide X-ray spectrum that has to be tailored to meet the required exposure parameters. To shape the spectrum, a mirror, a beam stop and absorbing filters are inserted into the X-ray beam. Between the mirror and the sample, a 5 mm thick beam stop is mounted in the centre of the synchrotron beam, to filter out most of the heat and low energy part of the spectrum. Additionally, to fine-tune the spectrum, four to sixteen layers of 17.5 μm thick aluminium foils are used in front of the mask. Between the working mask and the resist layer, an additional filter is placed. This contains additional two layers of 17.5 μm aluminium and 50-125 μm of polyimide (Kapton[®] HN – CMC 70050, CMC Klebetechnik GmbH, Frankenthal). The whole set of resist, filters and mask is mounted into a holder that is placed directly into the X-ray scanner. The scanner moves the holder in vertical direction through the horizontal line-shaped X-ray beam of the synchrotron source to get constant intensity exposure in the entire layout area. After depositing the required dose, the post exposure bake (PEB) takes place to perform the crosslinking of the exposed areas. The PEB is carried out on a conventional laboratory hot-plate.

The hotplate program used for the lenses in this thesis has been the following:

- Two hours ramping up the temperature to 66°C
- Keeping the temperature at 66°C for twenty hours
- Letting the sample to cool down to 22°C in 6 hours

In the next step, the unexposed resist residue is removed through chemical development. As mr-X is a negative resist, organic developer, propylene-glycolmonomethyletheracetat (PGMEA) is used for this purpose. Depending on the resist thickness, the development times varies from two times 60 minutes to three times 180 minutes, with the developer exchanged between

the steps. As last step of the development, a 60-minute isopropanol bath takes place, to make sure that all resist residues are washed away. After drying in a laboratory oven at 30 °C, the X-ray lens can be inspected. This is usually done with a standard light microscope. SEM-examination of the masks and optical microscopy inspection of the end results are proven to be sufficient to ensure the expected sidewall precision for the requirements of X-ray lenses [30].

3.3 Measurement of the refractive index for the lens materials

To be able to design a lens one has to know the refractive index of the lens material. As this parameter has not been known before with the necessary accuracy and as the chemical composition of the resist is a trade secret and may vary from batch-to-batch, a method had to be developed to measure the relation between photon energy and refractive index of the photo sensitive resist mr-X-50.

Figure 3-3 shows the basic setup of the measurement, simply based on Snell's law. The resist material whose refractive index is to be measured is patterned as an array of hundreds of columns with a square cross-section and an edge length of about 100 μm . This test object is placed in the nearly parallel beam of a synchrotron source. In front of the array, a pair of absorbing slits stops the incoming radiation down to form a beamlet of about the size of one column. This beamlet hits a row of the prisms and is by refraction divided into two separate beamlets. These beamlets travel through the row of prisms, then behind the array propagate and hit a detector.

With the measured values d and h and the number of the columns with a square cross section, positioned in one row precisely on the optical axis, one has all necessary parameters to calculate the refractive index of the material at the photon energy at which the measurement was performed. As for most experiments in this field the alignment and positional accuracy is exception-

ally crucial. The test object has to be precisely aligned with the optical axis of the whole setup.

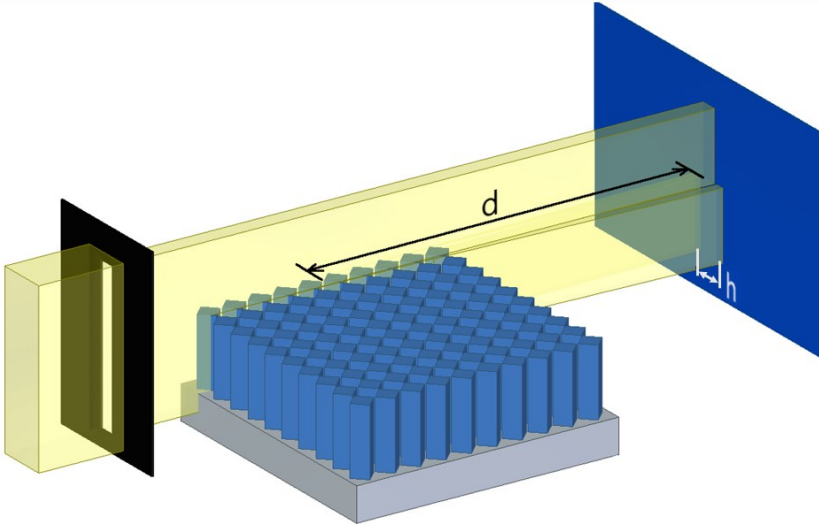


Figure 3-3: Sketch of the refractive index measurement setup; d is the test object and detector distance, h is the distance between the two separated parts of the beam at detector position

The deflection angle can be calculated as the arcus tangent from the deviation of the beamlets from the optical axis, and the detector distance from the test object, assuming the distance d being very large compared to the length of the row of columns:

$$\alpha = \tan^{-1} \frac{h/2}{d} \quad (3.1)$$

where α is the angle of deflection, $h/2$ is the halve distance between the two deflected beamlets on the detector perpendicular to the optical axis and d is the distance between detector and the test object. The value α is equal to the theoretical expected deflection based on Snell's law. With respect to the number of elements of the test columns N_{columns} , the refractive power can be numerically reconstructed using equation (3.2).

$$\alpha = N_{\text{columns}} * \delta_P \quad (3.2)$$

with the deflection angle δ_P caused by one column. Figure 3-4 shows the refraction of a ray hitting a prism with triangular cross-section, described by Snell's law. The incident ray is refracted at both of the material boundaries, first as penetrating the prism and secondly as it is exiting on the right hand side [22].

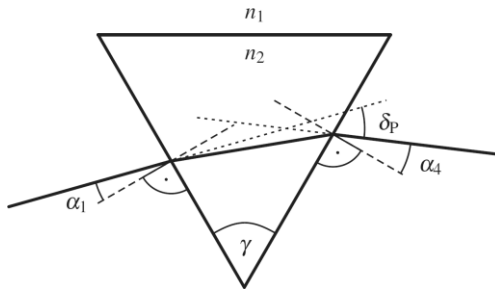


Figure 3-4: Sketch of a ray refracted when propagating through a triangular prism to show the principle used for the refractive index measurement

The deflection angle δ_P is calculated to be

$$\delta_P = \gamma - \alpha_1 - \arcsin\left(\frac{n_2}{n_1} \sin\left(\gamma - \arcsin\left(\frac{n_1}{n_2} \sin\alpha_1\right)\right)\right) \quad (3.3)$$

In the case of the columns used to measure the refractive index the opening angle is $\gamma=90^\circ$.

Measured data

The measurement took place at the Topo-Tomo beamline at the synchrotron source KARA. The test structure had 138 prisms in one 18 mm long row and its centre was 1287 mm away from the detector. The detector had an effective pixel size of 500 nm/pix. The resulting detector picture is shown in Figure 3-5.

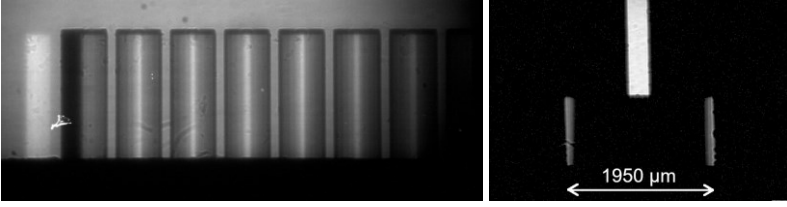


Figure 3-5: Refractive index measurement structures (400 μm high resist, column edge length 100 μm) layout 1337_00_A0 at 10 keV; radiography with the detector close to the structure (left) and with a structure to detector distance of 1.287 m (right)

As an example 10 keV photon energy will be considered in the following. Along the measurement, six rows have been examined. The measured distances d between the two deflected beamlets on the detector were 1950 μm , 1965 μm , 1947 μm , 1968 μm , 1947 μm and 1968 μm . The average distance $h/2$ from the optical axis at the detector plane is 979 μm with a standard deviation of 0.49 %. This results in a deflection angle of $\alpha = 0.04389^\circ$ using formula (3.1). The ratio of the length of the row of columns to the detector distance of 18 mm / 1287 mm ≈ 0.014 , thus the approximation in formula (3.1) is quite good. Taking the length of the test array into account, we get a deflection $\alpha = 0.04327^\circ$. Based on this a decrement of the index of refraction of $\delta = 2.736 \cdot 10^{-6}$. From the data set of decrements and photon energies, the decrement of the index of refraction of the SU-8 resist type mr-X-50 with 400 μm resist thickness can be interpolated as:

$$\delta = \frac{0.00027142 \text{ (keV}^2\text{)}}{E^2} \quad (3.4)$$

where E is the photon energy in keV. This experiment will be repeated multiple times for application requiring accurate refractive properties of the material. In this context, error bars will be established in the future.

3.4 Fabrication limitations

The main limitation of deep X-ray lithography today is the maximum achievable aspect ratio of the structures. Aspect ratio is the ratio between the height

and the edge length or diameter of an element. The taller an element is the more likely it will collapse or stick to its neighbours because of the acting capillary forces during drying after development see Figure 3-6. As it has been shown in chapter 2.4.2, absorption is a function of the material thickness, so less material means significantly less absorption in a lens. The height restriction of the prisms limits the useable aperture and thus in focusing applications limits the achievable minimal focal spot size.

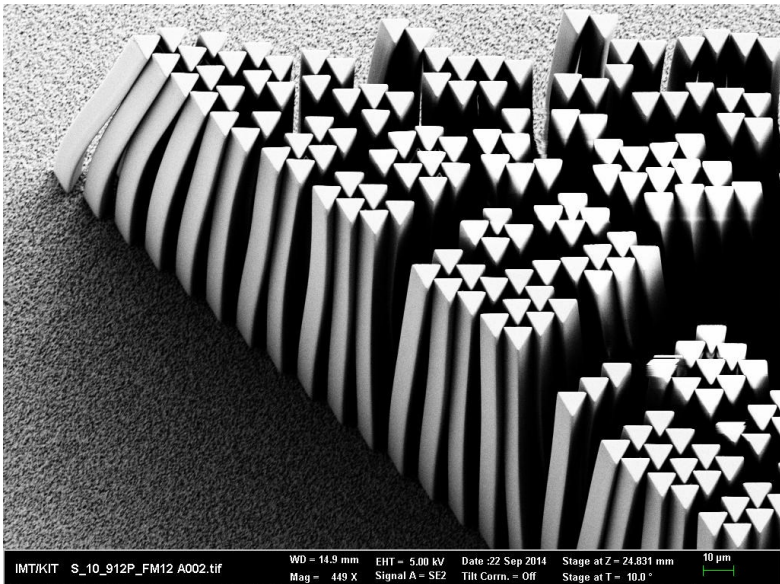


Figure 3-6: SEM image of prisms stuck together due to capillary forces occurring during drying after development

In the case of standard processing for prism structures an aspect ratio of 11 has been achieved in 2008 [31].

3.5 Reinforcement of XPLs

This work concentrates on focusing or enlargement of X-ray beams in vertical and in horizontal direction. In the case of prism lenses, this requires posi-

tioning two line-focus XPLs behind each other, rotated by 90° around the optical axis. Thus, for both lens halves, the height of the prisms has to be equal to the aperture of the optics, to get a square aperture. Additionally, as the absorption should be kept as low as possible, the cross section of the prisms has to be minimized. This requires fabricating much higher aspect ratios than ever before.

State of the art

Applying freeze-drying as the last step of fabrication can help realizing high aspect ratio microstructures. Freeze-drying avoids the formation of a meniscus between neighbour prisms during the drying process and thus capillary forces leading to a coagulation of the prisms. However, freeze-drying can only be used for small prism cross-sections, as adhesion problems between substrate and structure occur with larger cross-sections due to different coefficients of thermal expansion. Thanks to freeze-drying, a maximum aspect ratio of 30 was achieved for freestanding prisms pillars with $10\ \mu\text{m}$ edge length in 2015 [32].

As the substrate contains mostly more than only one lens, after development, the lenses have to be separated from each other. The separation of the individual lenses takes place using a regular wafer dicing saw. This device uses a water bath to submerge the substrate for the time of dicing to cool the saws' blade. Therefore, the capillary forces will act on the microstructures again, when submerging the substrate in the dicing bath. Completing the whole fabrication process wet-in-wet and then freeze-drying on the last step is practically not feasible at IMT, also with regard to the different liquids used in different process steps. Furthermore, the saws' vibrations and acting forces commuted by the liquid put a significant load on the structures further challenging the adhesion on the substrate. Consequently, freeze-drying cannot be the solution to produce very high aspect ratio prism structures.

Another partial solution – by introducing an exposed cover layer – led to a successful realization of aspect ratios of up to 60, shown in Figure 3-7 [22]. This lens is built up of $15\ \mu\text{m}$ edge length prisms, with $15\ \mu\text{m}$ gap between them.

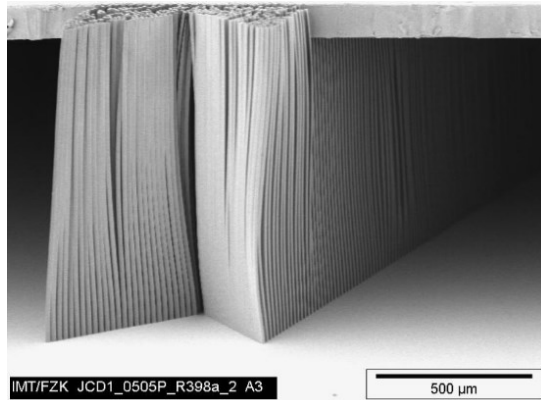


Figure 3-7: SEM image showing the impact of stabilizing with a cover layer [22]

Possible solutions

Two different solutions have been investigated within this work and will be shown in the following.

The first idea is to have a sponge-like matrix surrounding and connecting the lens elements. The only difference to the standard deep X-ray lithography method is the step of coating the resist. The open-pored matrix is soaked with resist instead of spin coating a flat substrate. After this step, the processing is more or less the same. The resulting matrix containing the microstructures would be more stable when handling the lens.

The second idea is simply having reinforcement structures embedded in the prism array. Figure 3-8 shows prisms connected with inclined supporting planes to lower the freestanding height of the prisms. One of the advantages of this approach, that the standardized lens fabrication process can be applied.

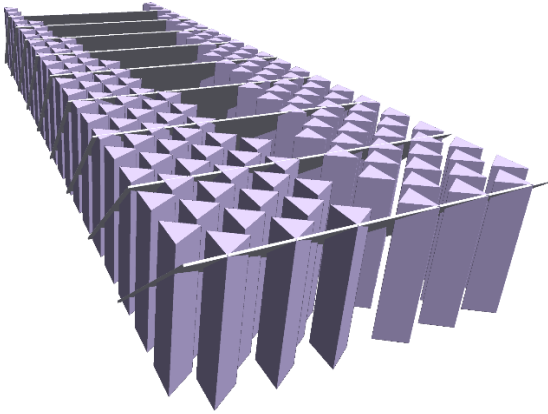


Figure 3-8: Principle of structural reinforcement using helping planes

Realisation of the matrix reinforcement

Two matrix materials have been tested as promising candidates for this approach. The first matrix is reticulated open cell polyethylene foam with the nominal porosity of 90 ppi (pores per inch). The SEM image of the raw sample can be seen in Figure 3-9. This particular sample has a thickness of 2 mm.

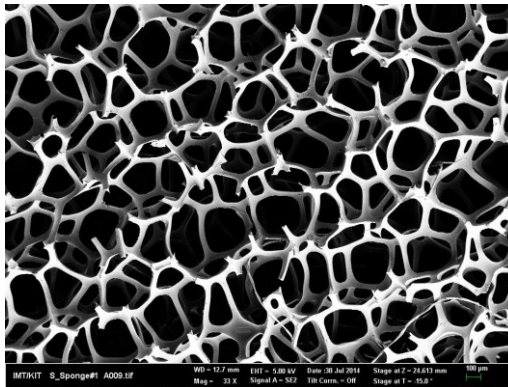


Figure 3-9: Reticulated polyethylene foam with 90 ppi nominal porosity as base material

As shown in Figure 3-10, the sample was successfully processed. Unfortunately, 90 ppi of porosity leads to 282 μm of nominal pore size, that is excessively high to carry out this experiment with prisms, so lamellas have been used as first test elements with a size of 25 μm along the short edge. An aspect ratio of 80 has been successfully achieved for grating lamellas with the thickness of 25 μm and a height of 2 mm.

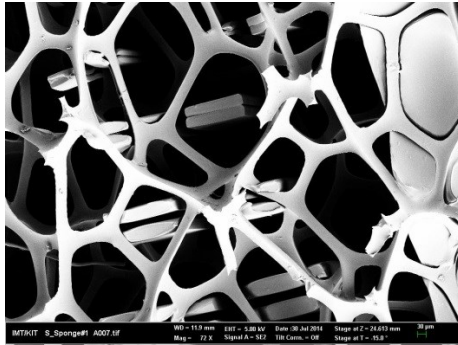


Figure 3-10: Reinforced lamella structures with an aspect ratio of 80 in polyethylene foam

As a second attempt reticulated vitreous carbon (RVC) foam has been used with more favourable 300 ppi of nominal porosity to be able to test the principle on XPLs with for example only 20 μm prism edge lengths as well. A SEM image is shown of the carbon foam in Figure 3-11.

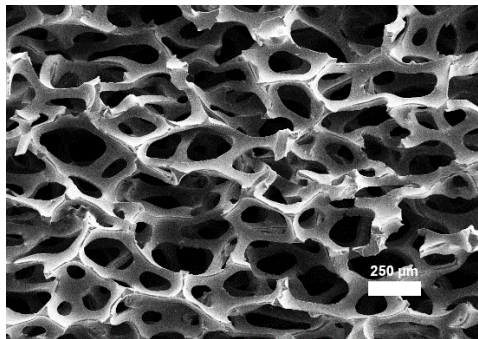


Figure 3-11: Reticulated Vitreous Carbon (RVC) foam with the nominal porosity of 300 ppi

As one can see in Figure 3-12 an XPL layout has been copied into a 5 mm thick RVC matrix. The edge length of the prisms is 20 μm ; the achieved aspect ratio is 250. This method has been patented in 2017 [33]. A major limitation of this method is the high background, due to the significant scattering introduced by the reinforcement matrix.

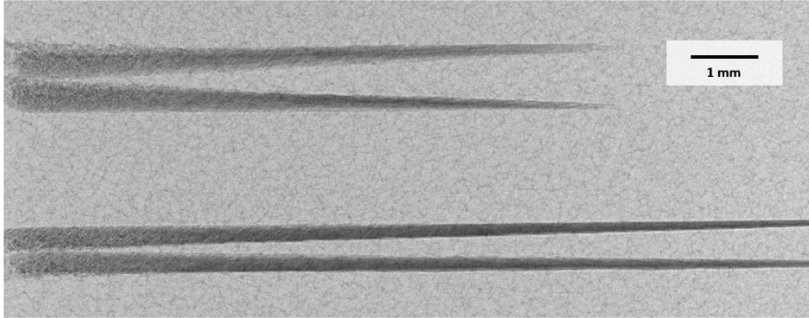


Figure 3-12: X-ray radiograph of two XPLs in 300 ppi RVC foam with an aspect ratio of 250

Realisation of supporting planes

Before a lens could be fabricated, using this method, the thickness, density, and inclination angle of the supporting planes had to be decided on. As transmission is essential, minimizing the loss is a high priority.

In the following, the overall absorption of the reinforcement system will be calculated. Beer-Lambert law gives

$$I_1 = I_0 * e^{-\mu\rho d} \quad (3.5)$$

where μ is the mass absorption or attenuation coefficient of the lens material, ρ is its density and d is the thickness of the penetrated material. Prior experiments have shown that with the aimed prism edge length of 20 μm , the columns are stable up to roughly 200 μm [31]. So a stabilizing structure pitch of 400 μm has been chosen, as the prism segments are supported at top and bottom. With these parameters and basic geometry principles, the optimal

inclination of the supporting planes to the substrate can be calculated. The computed result for a typical example setup can be seen in Figure 3-13. Supporting planes parallel to the substrate would obviously be optimal. However, such planes cannot be exposed lithographically.

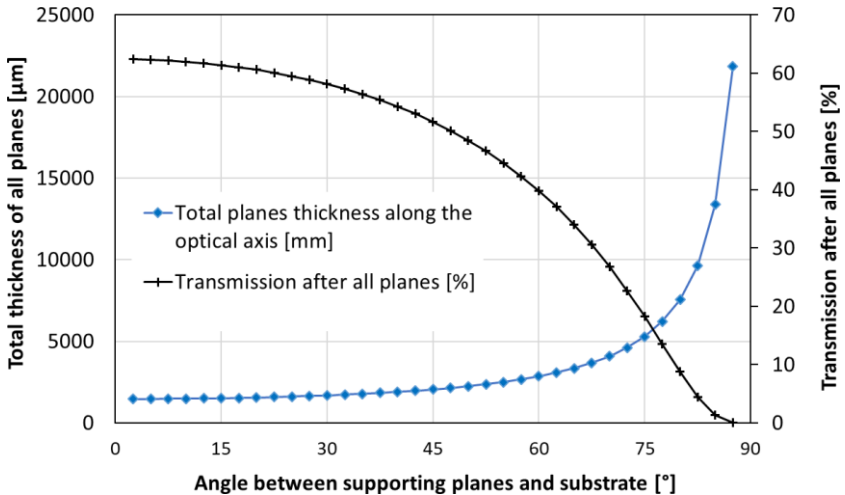


Figure 3-13: Example of the total transmission of 10 μm thick supporting planes for a 60 mm long optics made of mr-X-50 resist at 15 keV and 400 μm pitch

As at IMT inclined deep X-ray lithography exposure is restricted to $\pm 45^\circ$, the best achievable value has been chosen to 45° . Figure 3-14 shows a detail of the working mask used for the fabrication of the supporting planes. This particular mask has been made on 2.3 μm of Ti membrane, having the minimal Au absorber thickness of 24 μm .

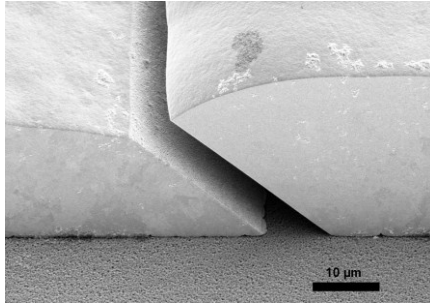


Figure 3-14: SEM image of the working mask for structuring the supporting planes (layout no. 1470_00_A0)

Figure 3-15 shows a side view SEM-image of 10 μm thick supporting planes and the supported prisms with 20 μm edge length. One can clearly see the straightness of the prisms all along the depth.

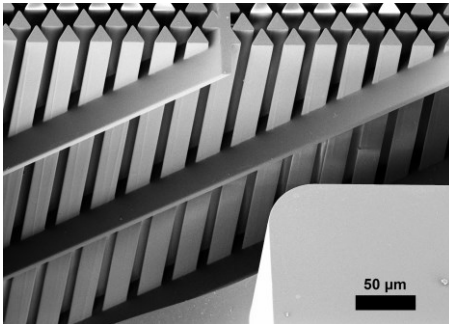


Figure 3-15: SEM-image of supporting planes, side view

Figure 3-16 shows a realisation of a prism lens with structural stabilizing planes and prisms. In the lower right part of the picture, an area without supporting planes is visible. In this area, the prisms are sticking together due to the capillary forces acting during the drying process. In the left side area with supporting planes the structure is ordered as it should be.

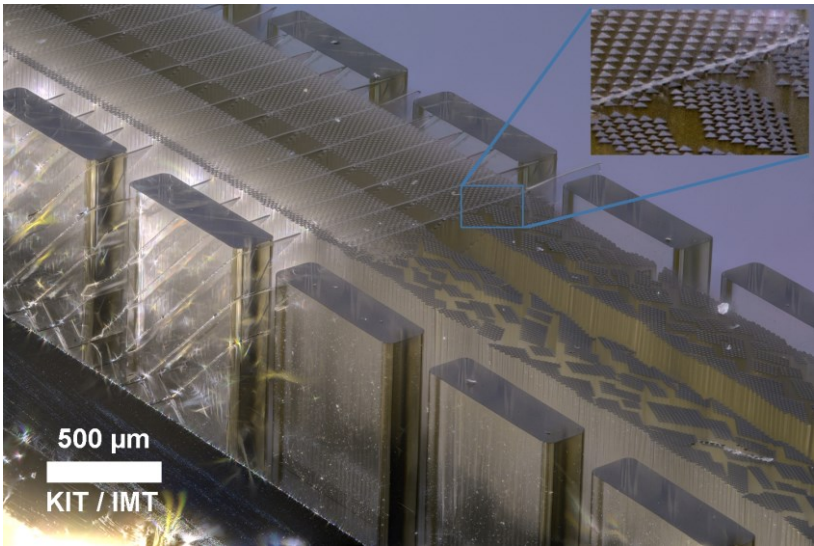


Figure 3-16: Focus-stacked photo of an XPL with supporting planes; the inset shows the border between an area with supporting planes (left) and an area with only prisms (right)

Figure 3-17 shows a top view of the prisms in Figure 3-16 with supporting planes (left side) and disordered without supporting planes (right side).

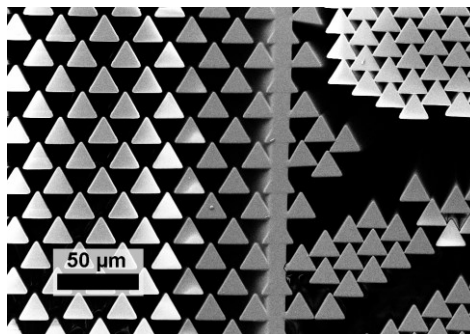


Figure 3-17: The effect of supporting planes on 20 μm prisms, top view

4 Focusing with X-ray prism lenses

For focusing X-rays above 8 keV, to use CRLs (Figure 4-1) is one of the possible choices, as it has been shown in chapter 2.4.

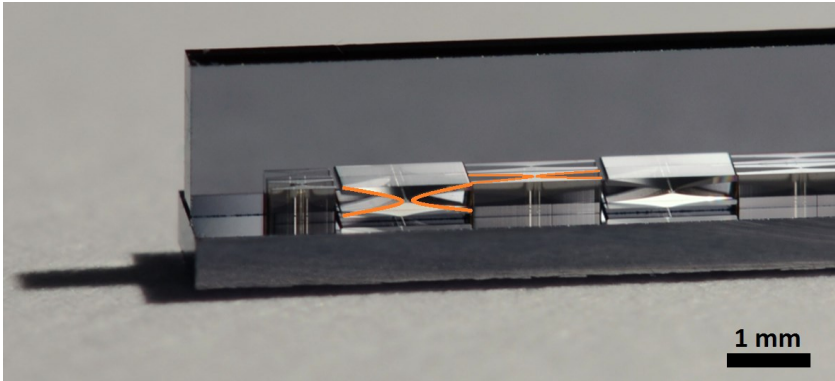


Figure 4-1: A spot focusing CRL mounted from two $\pm 90^\circ$ exposed line focus lenses

The main attribute making them well suited for this application is the decreasing absorption of the lens material for higher photon energies. Some CRLs achieved focal spot sizes in the 10 nm range [34]. The effective aperture of refractive optics is limited by absorption (Figure 4-2).

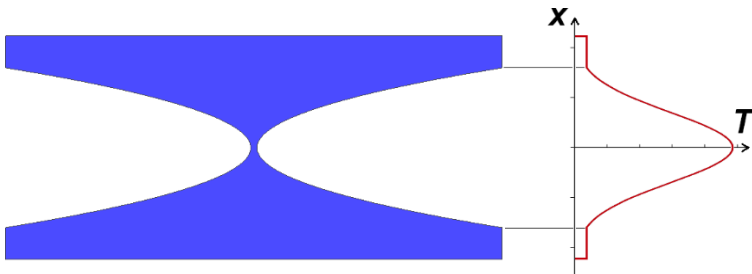


Figure 4-2: Transmission T of a CRL over the physical aperture A ; the effective aperture is smaller than the physical aperture

One way to address this problem is to use X-ray Prism Lenses (XPL) [1]. Depending on the application, XPLs can be designed for full field illumination of a sample in X-ray microscopy or also for illuminating a small focal spot. Up to this point, the focal spot size has been limited to the effective height of the cross section of the prisms. In the following, a method is shown how to overcome this limitation.

4.1 Aim and main challenges

The aim is to achieve the smallest possible focal spot size and at the same time to concentrate as many photons in its area as possible. In other words, to increase the photon density in the focal spot. The first aspect of the challenge is to achieve a small focal spot size. As shown in chapter 2.4.3 the focal spot size of XPLs is limited by the effective cross section of the prisms. Normally this means, that the prisms shall be as small in cross section as possible. On the other hand, the entrance aperture of the lens should be as big as possible, or in other words, the prisms have to be as tall as possible. Thus, the width and the height of the lens should be equal and maximized (see Figure 4-3). Additionally, the prism cross section should be minimized to reduce absorption.

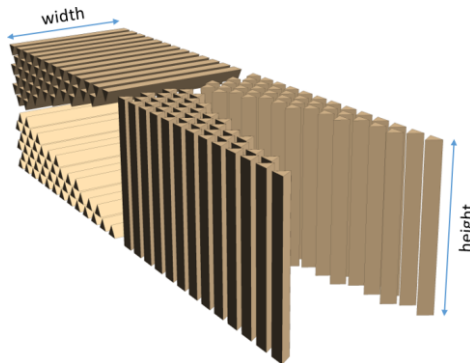


Figure 4-3: A model of a 2D crossed XPL for point focusing purposes, showing the height requirements for the individual lens halves

The main advantage of using XPLs instead of CRLs is the difference in effective aperture, as a result of the reduced material thickness in the outermost areas of the aperture. The main disadvantage is the limited focal spot size. The prism rows do not intrinsically focus the radiation. Each prism row of an XPLs only redirects the incoming beam towards the focal spot, thus accumulating intensity in the focal spot. Figure 4-4 shows the difference between a focussing CRL and a prims only redirecting the incoming beamlet.

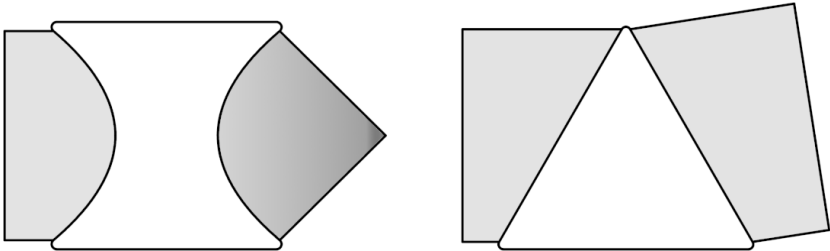


Figure 4-4: The difference in beam interaction visualized in the case of a CRL element (left) and an XPL element (right)

In short, the state of the art prism optics has a strict trade-off between spot size and effective aperture. To achieve a higher Spectral Intensity Enhancement (SIE) [35] and smaller focal spot size, a new approach had to be found to decouple the spot size from the prism cross-section.

4.2 New concept

As a solution, a system has been developed in which common XPL elements are combined with small, double-parabolic, concave elements (μ CRLs) with an aperture in the size of the prism height.

The basic idea of the design is to combine the beamlet redirecting behaviour of a prism row with the focusing capability of parabolic elements, so breaking down the problem to two sub-problems. With proper design, it can be achieved that a certain prism row of the XPL deflects the incoming beamlet precisely towards the focal spot and at the end of each prism row, a set of a

few μ CRLs focuses this beamlet to further reduce the focal spot size. Combining the two principles, the physical size of the prism cross-section is no longer the limiting the focal spot size. Figure 4-5 shows the proposed solution.

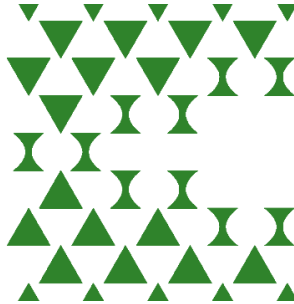


Figure 4-5: Proposed arrangement of the structures with double parabolic elements in each of the prism rows

Figure 4-6 shows a SEM image of the relevant part of an intermediate mask, used for the fabrication of such optics.

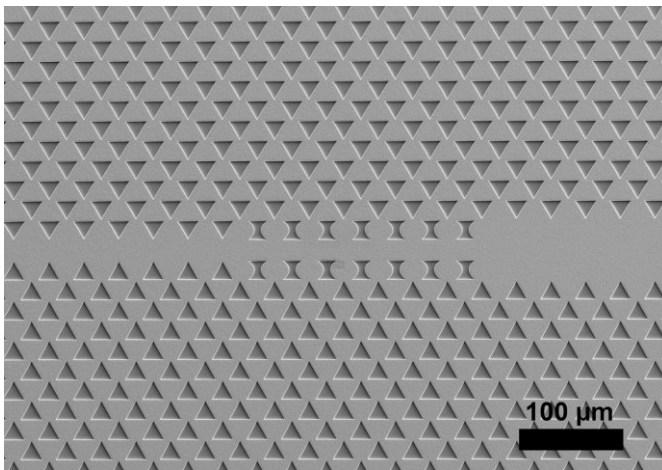


Figure 4-6: SEM image of a deep X-ray lithography intermediate mask, showing the prism rows plus μ CRLs focusing lens concept

Within this chapter we apply thin lens approximation, i.e. the length of the lens along the optical axis is negligible in respect to the focal distance. The working distance of a prism row for a very distant source point is:

$$f_{\text{prism row}} = \frac{h}{\tan(N_{\text{row}} \cdot \delta_p)} \quad (4.1)$$

where h is the distance of the prism row from the optical axis at the entrance aperture, N_{row} is the number of the prisms in the row and δ_p is the angle of deflection of a single prism. The focal length of a CRL is

$$f_{\text{CRL}} = \frac{R}{2 \delta N_{\text{CRL}}} \quad (4.2)$$

where R is the radius of curvature in the centre of the parabola, δ is the refractive index decrement of the lens material and N_{CRL} is the number of parabolic lens elements. To combine the two effects, for each single prism row the focal distance of the μCRLs is chosen to meet the XPLs focal plane.

Another aspect to consider is the transmission of a lens like this. The absorption of the whole system can be computed as the sum of the XPL and the μCRL absorption part.

The principle arrangement of a conventional XPL lens is shown in Figure 4-7. As a ray entering a prism row is deflected by the first prism by the angle δ_p , then travels to the next prism, is deflected again and so on, the optical path of the ray through the XPL is a polygon. This polygon can be approximated by a circle with a radius in the metre range.

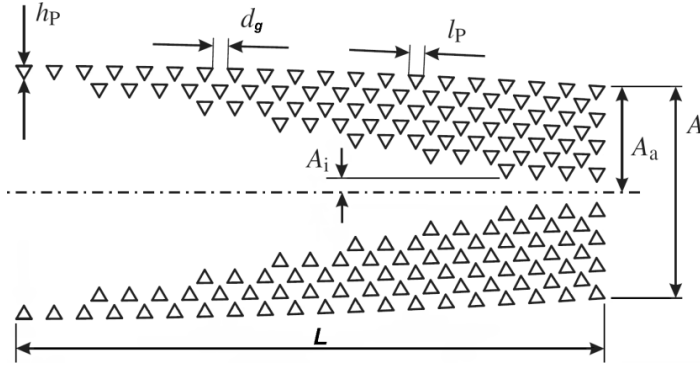


Figure 4-7: Principle drawing of a conventional XPL lens; h_P is the effective cross section height of a prism, d_g is the gap between prisms, l_P is the prism cross section edge length, A_i is the distance of the first prism row from the optical axis, A is the aperture, A_a is the half aperture and L is the total length of the XPL

The layout is designed that every single prism is rotated so that the base edge of it is parallel to the local incident ray. Fulfilling this criterion, the transmission of an ideal single prism is [22]

$$T_{\text{prism}} = \frac{1}{h_P} \int_0^{h_P} e^{-\frac{4\pi\beta E}{1.239} 2 \tan\left(\frac{\gamma}{2}\right) h} dh \quad (4.3)$$

where h is the distance of an incident ray from the tip of the prism pointing towards the optical axis, h_P is the height of the prism perpendicular to the optical axis, γ is the opening angle of the prism, β is the extinction coefficient of the prism material and E is the photon energy in keV. All the length units are measured in micrometres.

In practice, a zero radius corner or edge cannot be realised. Technically the X-ray lithography process adds fillets with a radius of about $r_P = 300$ nm to all edges. Figure 4-8 shows a prism with fillets. Only the prism area of height $h_P - d_0 - d_u$ will transmit the incoming rays to the wanted direction. Approximating the worst case all the light entering the rounded areas at the corners will be considered as lost, as it will be scattered in random directions.

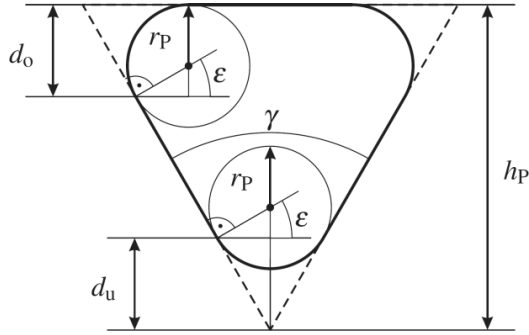


Figure 4-8: Cross section of a real life prism with fillets

Including all physical constrains to the layout design the transmission of a single, physically realisable prism is

$$\eta_{\text{prism}} = \frac{1}{h_P} \int_{d_u}^{h_P - d_o} e^{-\frac{4\pi\beta E}{1.239} 2 \tan\left(\frac{\gamma}{2}\right)h} dh \quad (4.4)$$

where

$$d_o = r_P \left[1 + \sin\left(\frac{\gamma}{2}\right) \right] \quad (4.5)$$

and

$$d_u = r_P \frac{\cos^2\left(\frac{\gamma}{2}\right)}{\sin\left(\frac{\gamma}{2}\right)}. \quad (4.6)$$

The overall transmission of one prism row can be calculated as

$$\eta_{\text{prismrow}} = \frac{1}{h_P} \int_{d_u}^{h_P - d_o} e^{-N_P \frac{4\pi\beta E}{1.239} 2 \tan\left(\frac{\gamma}{2}\right)h} dh \quad (4.7)$$

where N_p is the number of prisms in the particular row. As the transmission for a complete XPL:

$$\eta_{\text{XPL}} = \sum_{n=1}^{N_{\text{row}}} \left[\frac{1}{h_p} \int_{d_u}^{h_p-d_o} e^{-N_p(n) \frac{4\pi\beta E}{1.239} 2 \tan\left(\frac{\gamma}{2}\right) h} dh \right] \quad (4.8)$$

In the following, the absorption of the μCRLs will be investigated. Figure 4-9 shows the difference between an ideal and a real CRL element.

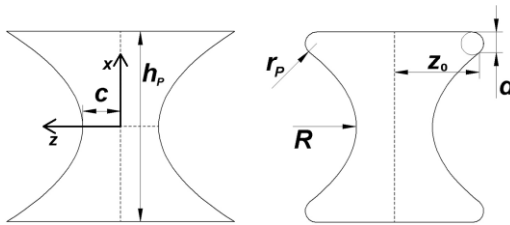


Figure 4-9: Cross section of an ideal (left) and real (right) CRL element

Regarding to fillets the same applies as before. With the radius of curvature in the parabolas' apex R and the half of the web c , the height z at the corners of the perfect parabola is

$$z = \frac{x^2}{2R} + c = \frac{(h_p/2)^2}{2R} + c \quad (4.9)$$

with the x -direction along the optical axis, the z -direction perpendicular to it and the origin positioned in the centre of the lens element. The slope of the parabola is

$$z' = \frac{x}{R} \quad (4.10)$$

and the distance s between the centre point of the fillet to the intersection of the rounding and the parabola itself along x is

$$s = r_p \sin \left(\tan^{-1} \frac{x_0}{R} \right) \quad (4.11)$$

where x_0 is the distance between the optical axis and the intersection of the parabola and the fillet

$$x_0 = \frac{h_p}{2} - r_p - s = \frac{h_p}{2} - r_p \left[1 + \sin \left(\tan^{-1} \frac{x_0}{R} \right) \right]. \quad (4.12)$$

In other terms the effective height d of a fillet along x is

$$d = s + r_p = r_p \left[1 + \sin \left(\tan^{-1} \frac{x_0}{R} \right) \right] = r_p \left[1 + \frac{\frac{x_0}{R}}{\sqrt{\left(\frac{x_0}{R}\right)^2 + 1}} \right]. \quad (4.13)$$

As the intersection point is calculated from the equation of the circle and the parabola

$$a^2 x + c = \sqrt{R^2 - [x - (A - R)]^2}. \quad (4.14)$$

$$\frac{x^2}{2R} + c = \sqrt{R^2 - [x - (x_o + s)]^2} + z_o - z_1. \quad (4.15)$$

with

$$z_1 = \frac{sR}{x_o}. \quad (4.16)$$

The overall transmission of one row of parabolas without fillets is

$$\eta_{\mu\text{CRLrow(ideal)}} = \frac{2}{h_p} \int_0^{h_p/2} e^{-N_{\text{CRL}} \frac{4\pi\beta E}{1.239} \left(\frac{h^2}{2R}\right)} dh \quad (4.17)$$

and with fillets is

$$\eta_{\mu\text{CRLrow}} = \frac{1}{2(h_P - d)} \int_{d-h_P}^{h_P-d} e^{-N_{\text{CRL}} \frac{4\pi\beta E}{1.239} 2(ah^2+c)} dh \quad (4.18)$$

with the tangent at the intersection is

$$2ax = \frac{d}{dx} \sqrt{R^2 - [x - (A - R)]^2} \quad (4.19)$$

concluded

$$2ax = \frac{A - R - x}{\sqrt{R^2 - (R - A + x)^2}} \quad (4.20)$$

As the transmission for the complete section of μCRLs ending up in

$$\eta_{\mu\text{CRL}} = \sum_{n=1}^{N_{\text{row}}} \left[\frac{1}{2(h_P - d)} \int_{d-h_P}^{h_P-d} e^{-N_{\text{CRL}(n)} \frac{4\pi\beta E}{1.239} 2(ah^2+c)} dh \right] \quad (4.21)$$

The transmission of the whole lens is

$$\eta_{\text{lens}} = \eta_{\text{XPL}} \cdot \eta_{\mu\text{CRL}} \quad (4.22)$$

4.3 Realization

Two layouts (IMT no. 1351_00_A0 and no. 1574_00_A0) have been developed and two sets of lenses have been fabricated within the project. For the first attempt, layout 1351_00_A0 has been designed for three different photon energies, namely 15.816 keV, 17.764 keV and 21.747 keV. For each photon energy, four different optics have been realized varying in prism size with 8 μm , 10 μm and 20 μm edge lengths. Besides this, a fourth set of lenses was included as a combination of 20 μm edge length prisms with matching

μ CRLs, overall counting twelve individual lenses. The layout can be seen on Figure 4-10. The prism height is $150\ \mu\text{m}$ without supporting planes.

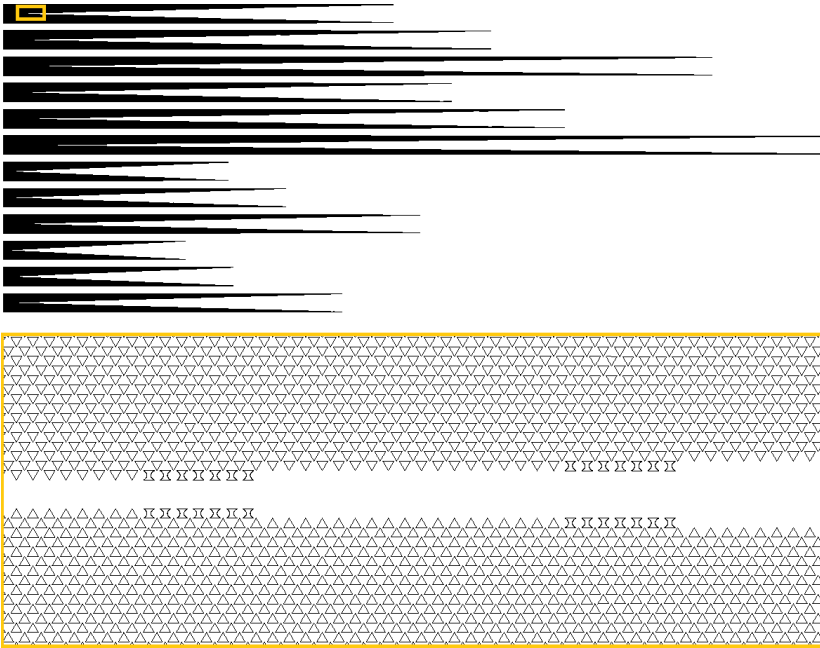


Figure 4-10: Overall image of layout 1351_00_A0 (top), a magnified image showing the combination of prisms and μ CRLs (bottom)

As for the second set of lenses, a new layout (IMT no. 1574_00_A0) has been developed, with the introduction of supporting planes. In this way, the vertical prism height limitation has been overcome. The lenses are made for a working distance of 400 mm and for the energies shown with the layout in Figure 4-11. The white rectangular blocks aside the prism fields are important for the supporting planes. These structures are relatively big compared to the prism cross section and were introduced to protect the prisms from any damage during processing, especially during dicing. Furthermore, these blocks serve as an anchor for the supporting planes. The lenses have been made $800\ \mu\text{m}$ tall, with a set of supporting planes.

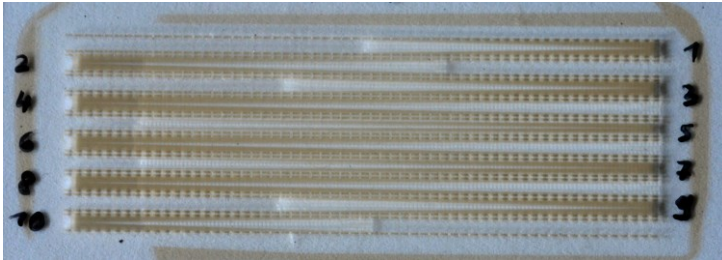
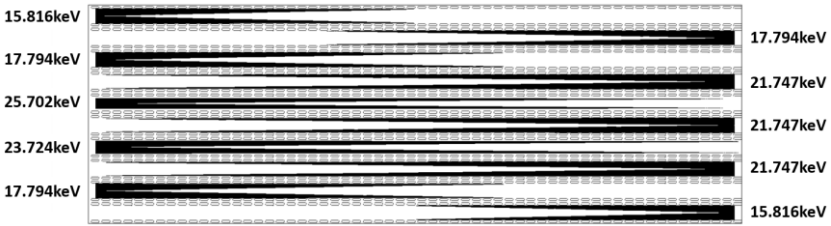


Figure 4-11: Image of layout 1574_00_A0 (top) and a photograph showing the finished glass substrate, carrying ten lenses

Figure 4-12 shows SEM images of the intermediate mask of layout 1574_00_A0.

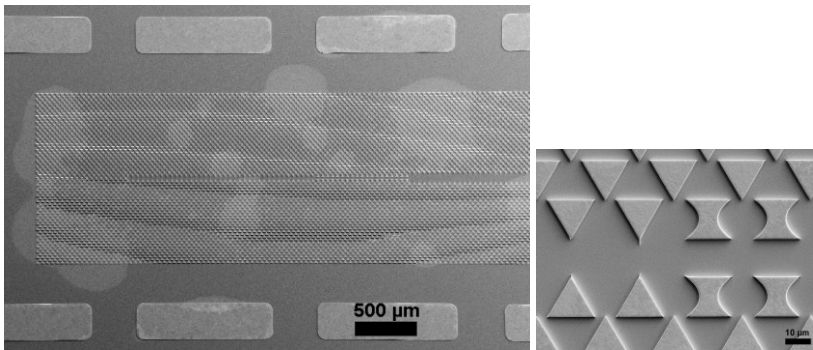


Figure 4-12: SEM image of the mask for layout 1574_00_A0 (left), magnified (right)

4.4 Results

In simulations based on a setup with a point source model, a focal spot size $< 1.5 \mu\text{m}$ FWHM has been achieved, using 60° -prisms with $20 \mu\text{m}$ edge length, combined with $17.3 \mu\text{m}$ high double parabolic elements (μCRLs), see Figure 4-10. The lens 1351_00_A0 #3 used in the simulations, has been designed for 15.816 keV and contains an integer number of identical prisms in every row and therefore the working distance for every row can result in only discrete values. Consequently, this leads to an increased focal spot size. The $\sim 1.5 \mu\text{m}$ size is the result of this limitation.

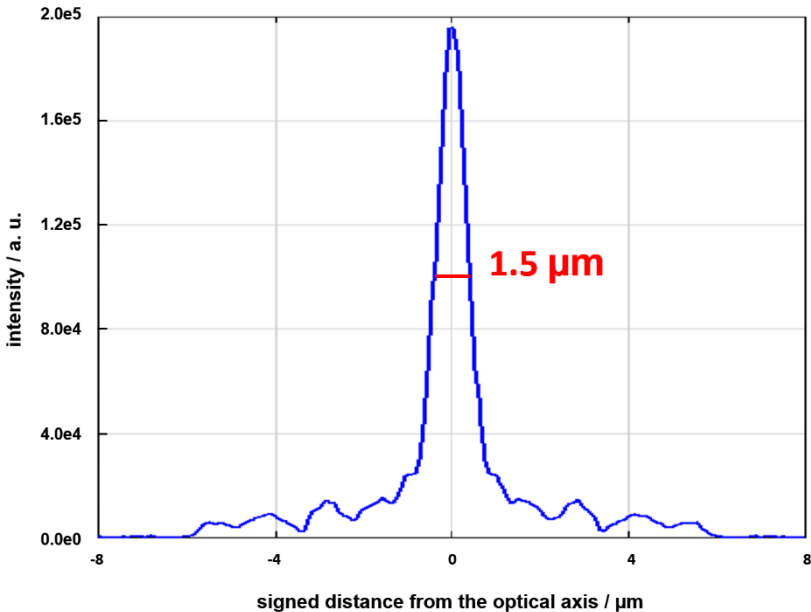


Figure 4-13: Raytracing result on the focal spot size of lens 1351_00_A0 #3 that combines $20 \mu\text{m}$ edge length prisms with $17.3 \mu\text{m}$ high μCRLs , using a point source model

Further simulations were calculated to investigate the influence of a real source and beam line optics to the overall results.

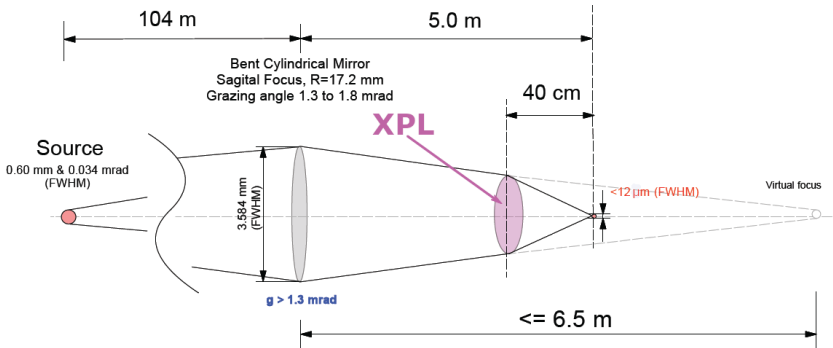


Figure 4-14: Schematic of the optical layout of SPring-8 beamline BL35XU at the time of the experiment including a pre-focusing mirror and the XPL. The beam propagates from left to right.

Beamline and source data is shown in Figure 4-14. The setup uses a pre-focusing mirror.

Figure 4-15 shows the results of a simulation using a real source model of the horizontal direction of the beamline BL35XU at the SPring-8 synchrotron source. The simulated focal spot size is $\sim 9.3 \mu\text{m}$ FWHM. The simulated overall transmission of the lens was 77 %. For a CRL with the same 2 mm entrance aperture, with the same focal distance of 400 mm designed for 15.816 keV the overall transmission would only be 14 %.

The XPL has been tested at SPring-8 in the beamline BL35XU. For the simulated XPL of lens 1351_00_A0 #3, a focal spot size of $15.1 \mu\text{m}$ (full width half maximum) and a transmission of 78 % have been measured in acceptable agreement with the simulations as it is shown Figure 4-16.

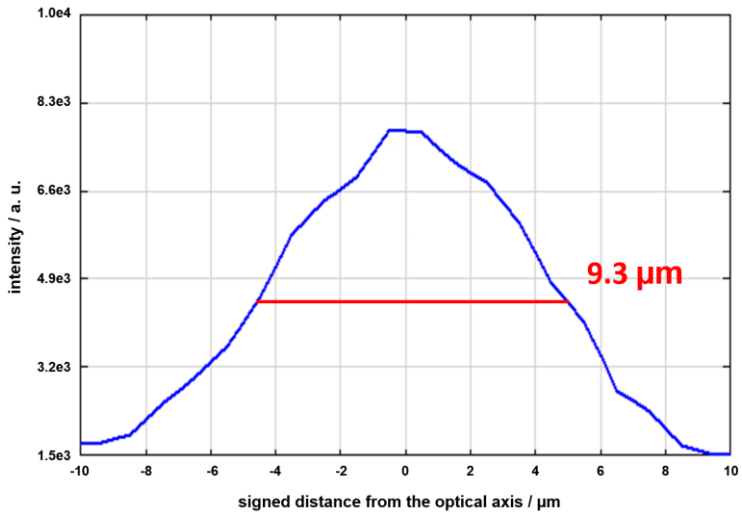


Figure 4-15: Raytracing result on the focal spot size of lens 1351_00_A0 #3 that combines 20 μm edge length prisms with 17.3 μm high μCRLs , based on a real source model

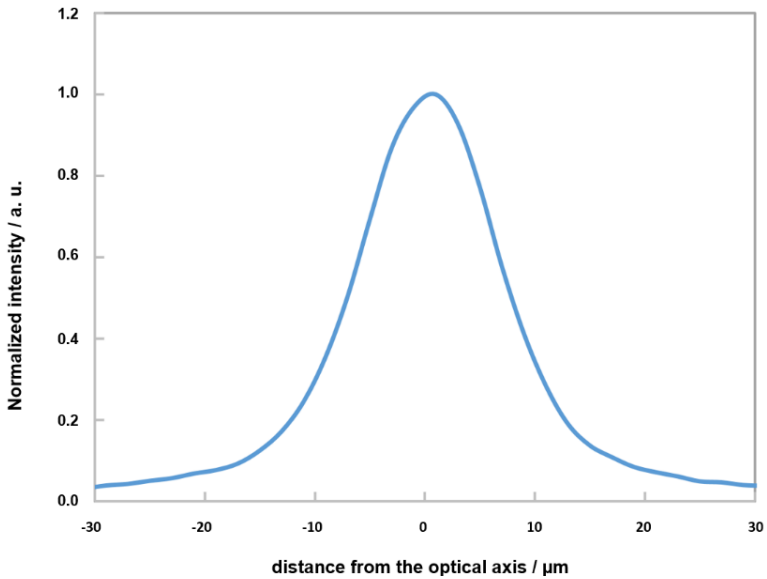


Figure 4-16: Measurement data of lens 1351_00_A0 #3

Regarding to the second layout (1574_00_A0) and 800 μm structures realised with supporting planes, the measurement data shows significantly more $\sim 80\%$ stray light background, as shown in Figure 4-17. A focal spot size of $\sim 20\ \mu\text{m}$ (full width half maximum) and a transmission of $>60\%$ have been measured.

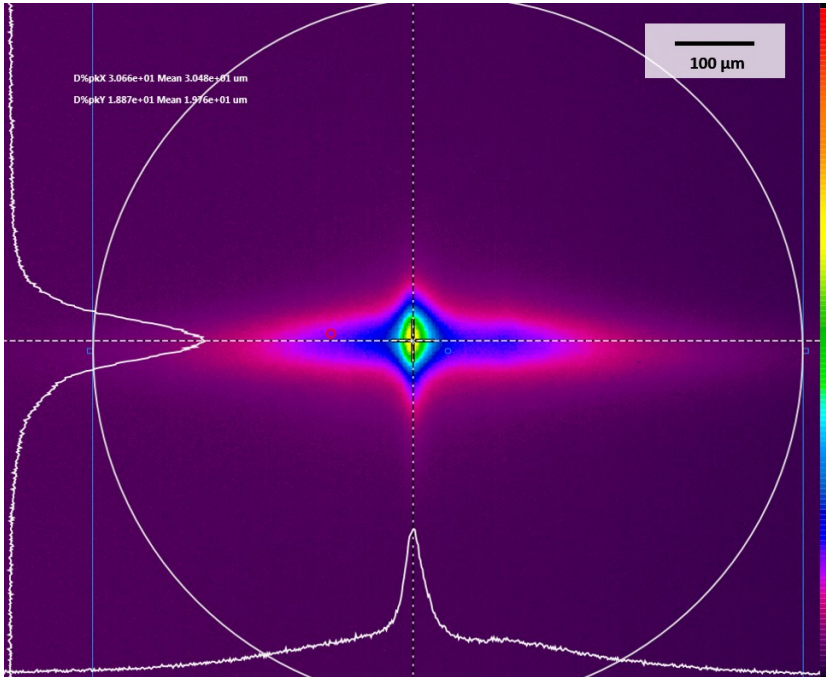


Figure 4-17: Measurement data of lens 1574_00_A0 #3, showing a focal spot size of $\sim 20\ \mu\text{m}$ FWHM

4.5 Summary focusing prism lenses

It has been shown, that with proper design, wide aperture focusing optics can be successfully fabricated as a combination of prisms and μCRLs . The newly designed optics provides major advantages in transmission and acceptable

incident beam size. Although in the work only one-dimensional (line focusing) cases have been covered, there is no limitation for a two-dimensional (point focus) application.

The supporting planes are introducing a significant amount of stray light. In a focusing application stray light is disadvantageous, in other applications (e. g. full field microscopy) might even contribute to a homogeneous illumination.

Further development possibilities would be to overcome the limitations related to the integer number of prisms in each single row. The radius of the μ CRLs as well as the angle of the prisms could be fine-tuned in a two-stage computation. When in the first pass the necessary prism number is established, based on this value the above mentioned parameters, i.e. the prism angle could be tailored in a way that the working distance of the XPL would perfectly fit the requested value.

5 **Condenser optics for full field microscopy**

Microscopy is a technique to investigate objects, mainly surfaces of objects that cannot be seen with the naked eye. In the field of X-ray microscopy, this investigation is not limited to only the surface, as X-rays penetrate materials easier than visible light. Besides this, X-ray microscopy can provide better spatial resolution than conventional optical microscopy, as the wavelength of X-rays is magnitudes smaller than for visible light, leads to a much smaller diffraction limit. In the following, the discussion will focus only on full field microscopy using a dedicated imaging optical element (objective lens) [36].

In Figure 5-1 shows a full field X-ray microscope. The setup includes an X-ray source, optional illumination optics, a sample, an objective lens imaging the sample to the scintillator plane of a detector system. The scintillator converts the X-rays into visible light and the detector system images the visible light image of the sample to a CCD-detector, which converts the light into electrical signals.

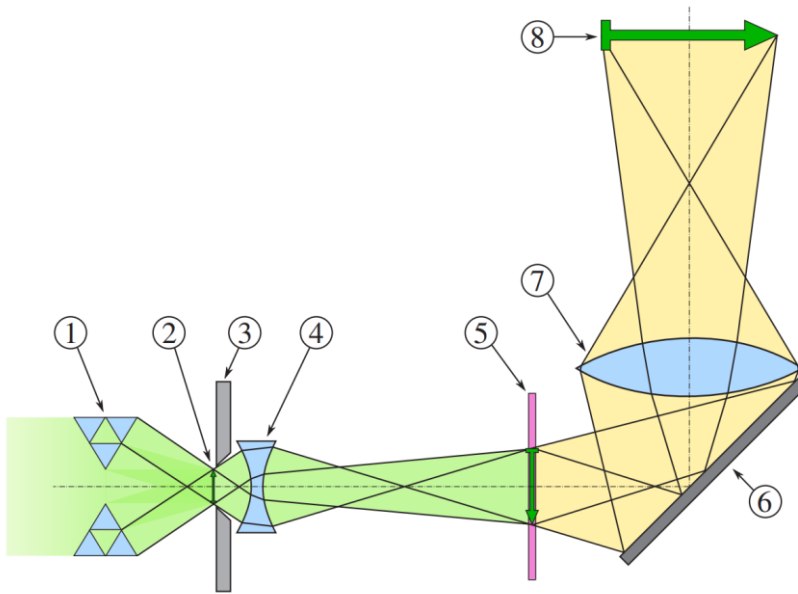


Figure 5-1: Full field X-ray microscope setup; 1: condenser lens, 2: sample, 3: aperture, 4: objective lens, 5: scintillator, 6: 45° deflection mirror, 7: conventional microscope objective, 8: CCD-detector [37]

In this chapter the design of an illumination optics will be explained, that is tailored to one specific objective lens.

5.1 Aim and main challenges

The purpose of the illumination optics is twofold. On one hand, it has to collect and distribute homogeneously as many photons as possible onto the sample. On the other hand, each point of the sample must be illuminated, that it radiates in such a way, that it fully illuminates the entrance aperture of the objective. The ray distribution leaving the sample has to be accepted by the imaging optics.

The advantage of using a condenser is twofold as well. Thanks to the higher number of photons passing through the sample, the acquisition time can be shorter. Secondly, the resolution b_{\min} of the image increases as well with the optimized angular ray distribution. Based on the Rayleigh criterion, for round objectives the following applies:

$$b_{\min} = \frac{1.22\lambda}{NA_{\text{condenser}} + NA_{\text{objective}}} \quad (5.1)$$

where λ is the wavelength and NA the Numerical Aperture

$$NA = n * \sin \frac{\alpha}{2} \quad (5.2)$$

where α is the angular aperture and n is the refractive index of the medium surrounding the lens. The Abbe diffraction limit is

$$b_{\min} = \frac{\lambda}{2NA} \quad (5.3)$$

if the numerical aperture of the condenser and the objective are equal [38].

CRLs for the X-ray regime are thick lenses with lengths easily up to 100 mm and physical apertures mostly in the range of only a few hundred micro metres. The ratio of aperture and lens length is fairly small. As a consequence, the acceptance angle changes from point to point especially at the outermost areas of the aperture. Therefore, it has to be computed for every point of the field of view. In Figure 5-2 one can see the typical acceptance regime of a CRL used as an objective lens. As it is shown, there is a significant difference in the angular distribution of accepted rays for points more distant to the optical axis.

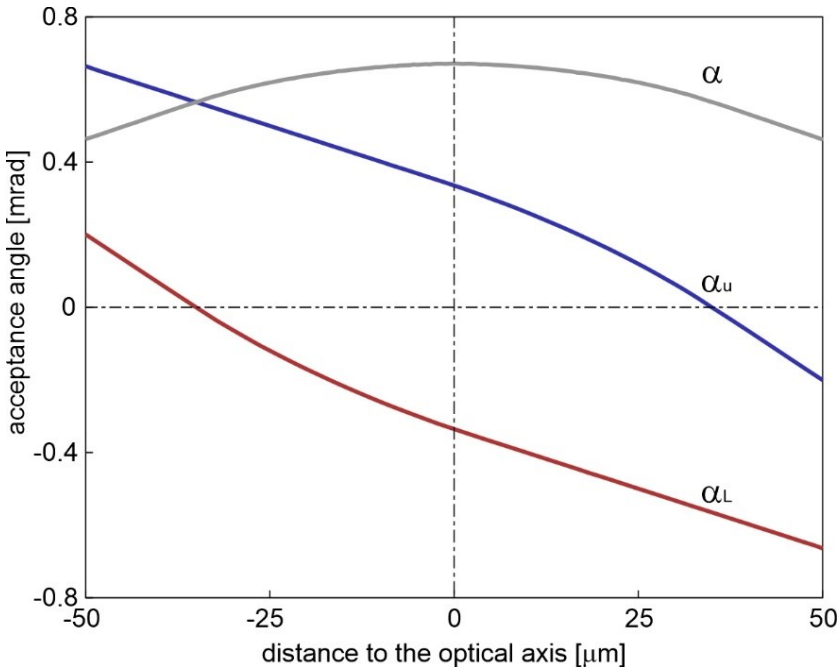


Figure 5-2: Example of the angular acceptance α of a CRL objective lens, α_u shows the uppermost, α_L shows the lowest ray entering the aperture [37]

As shown by the uppermost and lowest ray, both the divergence and the direction change from point to point from the centre towards the edges of the field of view. The reason for this is a combination of the fact that the field of view of the lens is not significantly smaller than the entrance aperture of the CRLs and that the lens is very long.

If an experiment relies only on the raw, slightly divergent beam of a synchrotron source, each point of the sample will contribute with nearly only one angle to the imaging. Such a microscopy setup looks like full field imaging, but in reality is a shadow projection setup with a twofold lower resolution compared to a real full field microscope. However, the resolution does not have to be sacrificed if the illumination is well adapted to the acceptance

angles of the imaging optics, namely the spatial and angular distribution of the optical radiation has to be optimised.

Nowadays, many options are given to concentrate the photons of the source onto the sample, although most of these do not provide an optimal solution, as a full-field microscope condenser. In many experiments one can see a CRL being used as illumination optics, with the sample simply placed after it, off focus, so the beam covers the whole object [39].

Dedicated condensers, for example poly-capillaries [40] are no optimal solutions either. These optics redirect the incoming beam by multiple reflections in bent capillaries without changing the divergence of the beamlets. A consequence is their fairly short working distance, mostly not compatible with the acceptance profile of long CRL lenses. Furthermore, the efficiency of poly-capillaries decreases for photon energies above about 15 keV, as their reflectivity lowers for higher energies.

Another possible condenser would be a straightforward standard XPL. Despite the fact that the redirection of light would certainly be better than using a simple off-focus CRL, most of the light brought to the sample would not contribute to the image, as most of the beamlets hitting the sample would not enter the objective lens and would not reach the detector.

5.2 New concept

As a solution for an optimized condenser a system has been developed comparable to the one explained in chapter 4. The condenser optics is built up from conventional prisms and μ CRLs, their number changing from prism row to prism row, dependent on the local optical requirements. The main difference is that for focusing double-concave lenses have been used, whereas in this case double-convex lenses were used as μ CRLs, to achieve the required beam distribution (Figure 5-3).



Figure 5-3: Drawing of the proposed arrangement of the structures

Two main design requirements have to be fulfilled. First, every prism row points towards an individual target height at the objectives entrance aperture. Second, the local beamlets' divergence is adapted to the accepted angular distribution at the entrance point of the objective CRL. To meet the target height at the objectives entrance aperture, the number of necessary prisms in the actual row can be computed exactly as explained in chapter 4. The only difference is that in this situation instead of aiming at the optical axis at the working distance, now the target is a certain point at the entrance aperture of the imaging lens.

Then, looking at a specific prism row of the condenser, the angular range of rays in the local beamlet is defined, which can pass the objective successfully. To cover as much as possible of this range, the beamlet leaving a prism row will be diverted by multiple biconvex μ CRL elements according to the necessary angular range at this point.

The entrance aperture $A_{\text{condenser}}$ and the working distance $wd_{\text{condenser}}$ of an XPL condenser are related to the entrance aperture $A_{\text{objective}}$ of the objective and the working distance $wd_{\text{objective}}$ between the sample and the objective CRL via

$$\frac{wd_{\text{condenser}}}{A_{\text{condenser}}} \approx \frac{wd_{\text{objective}}}{A_{\text{objective}}} \quad (5.4)$$

Since many parameters enter into the design of a condenser XPL, such as the photon energy, the lens material, the distances between source, sample and objective lens, as well as the parameters of the objective CRL. Thus, the optimal solution cannot be achieved in a straightforward way, but iteratively. Several condenser layouts were realized. The characteristic parameters of the XPL condensers are listed in appendix A.

5.3 Realization

A layout (IMT no. 1482_00_A0) has been developed and a set of lenses has been fabricated within the project. 18 half-lenses have been produced on one single substrate, see Figure 5-4. They have been fabricated with supporting planes. Every lens half was designed as a combination of varying edge length prisms with matching μ CRLs, with slightly different working distances. As this type of lens cannot be cross-mounted, as it has been shown in Figure 4-1 for CRL objective lenses, the two lens halves for vertical and horizontal direction have to be mounted after each other, resulting in spatial distance between them along the optical axis. As the two half-lenses have to illuminate the same sample plane, it is necessary to have a different working distance for each of the half-lenses.

A short summary of the basic parameters of the condensers can be seen in Table 5-1. More detailed parameters of the lens layout can be found in appendix A.

Table 5-1: Input parameters for the condenser design regarding to the objective lens

Lens ID	Objective ID	Photon energy / keV	Working distance / mm		FoV sq. at sample position / μm	Sample-objective distance / mm	Condenser aperture / μm	
			1st D	2nd D			1st D	2nd D
1	1278 #4	17.4	453	483	100	77	1000	1060
2	1278 #6	30	585	650	100	65	1000	1100
3	1465 #2	13	263	294	150	60	1000	1100
4	1465 #5	17.4	117	156	400	80	1000	1200
5	1465 #7	24	587	642	150	150	1000	1080
6 (R6 μm)	1465 #11	30	658	720	150	150	1000	1080
7	WürzB	9.3	492	524	80	70	1000	1080
8 (R2 μm)	1465 #11	30	658	720	150	150	1000	1080

As it can be seen in Figure 5-4, the lens layout has been designed including side blocks to keep the possibility of combining it with supporting planes for high aspect ratio prisms.



Figure 5-4: Overall image of layout 1482_00_A0. The two first half-lenses in the top left corner are without, all other half-lenses with the inclusion of side blocks as anchors for the supporting planes

Figure 5-5 shows an image of the working mask that has been used for the exposure of the resist. As most of the masks, this particular one as well has been made on 2.3 μm thick titanium foil as the carrier membrane.

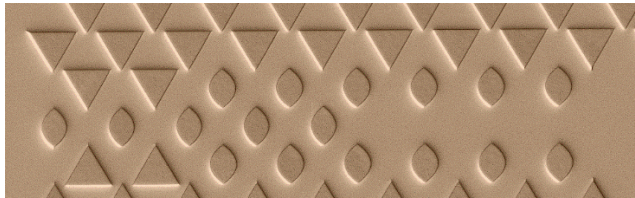


Figure 5-5: Partial SEM image showing the innermost area of the working mask of layout 1482_00_A0

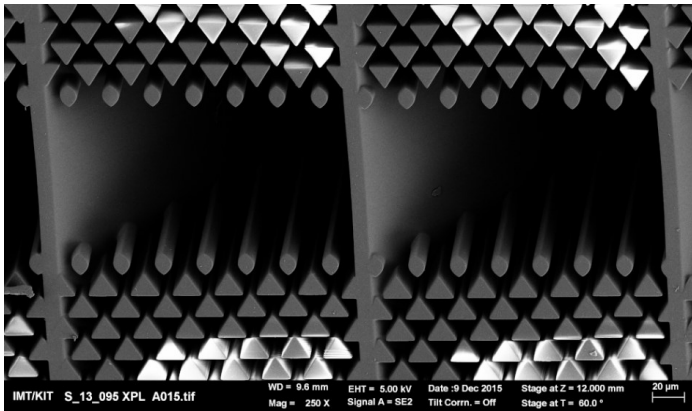


Figure 5-6: SEM image of one lens of layout 1482_00_A0

Figure 5-6 shows the completed lens combined with some supporting planes allowing for an overall height of $816\ \mu\text{m}$, thus a two-dimensional $816\ \mu\text{m}$ square entrance aperture is feasible. With a prism edge length of $18\ \mu\text{m}$, this means an aspect ratio of 45.

5.4 Results

The 3rd lens of layout 1482_00_A0 (see Table 5-1) will serve as an example of the simulation results. For the simulation as in the other cases, ZEMAX has been used. All of the relevant parameters are listed in Table 5-1 and appendix A. The lens has $20\ \mu\text{m}$ edge length prisms and adapted biconvex μCRLs . The overall transmission of the lens is 54 %. Figure 5-7 shows the simulated behaviour of the lens. On the left side of Figure 5-7 one can see the incident $200\ \mu\text{m} \times 1000\ \mu\text{m}$ beam (horizontal x vertical) at the condensers' entrance aperture whilst on the right side the concentrated beam at sample position covers the expected $150\ \mu\text{m} \times 150\ \mu\text{m}$ field of view.

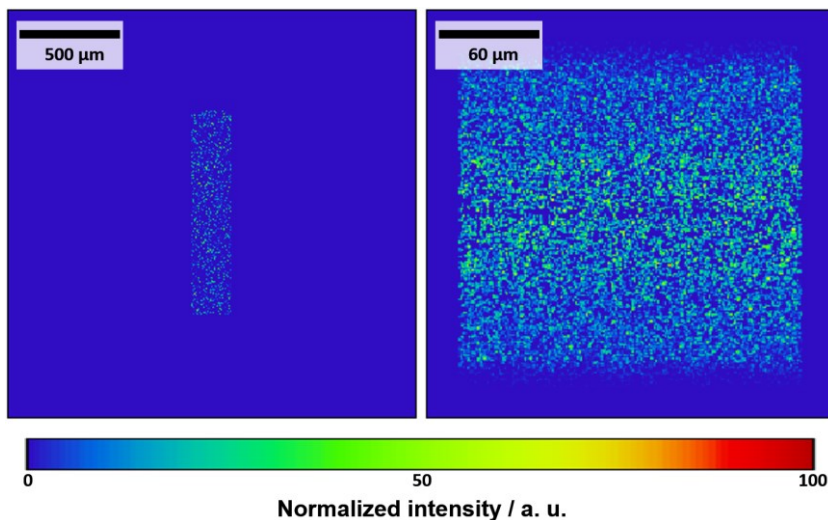


Figure 5-7: Simulation results of the 3rd lens of layout 1482_00_A0, designed for matching the 2nd objective lens of layout 1465_00_A0; incident beam at condenser entrance aperture (left) and beam cross section at sample position (right)

The simulation only shows the effect of the condenser concentrating the incoming beam in the sample plane, compressing it mainly in vertical direction as it was planned and expected. The adaptation of the angular distribution to the angular acceptance of the objective is not included in the figure.

The experiment to determine the performance of the optics took place in Hamburg, at the synchrotron source of PETRA III at DESY. Working together with the beamline scientists of the beamline P05 useful data has been acquired and demonstrate the first step in the development of such condenser optics.

The experiment was conducted at 17.4 keV, using the adapted objective lens. Additionally, all of the following images have been captured at detector position in a true X-ray microscope setup. Figure 5-8 shows that the illumination is far from being homogeneous.

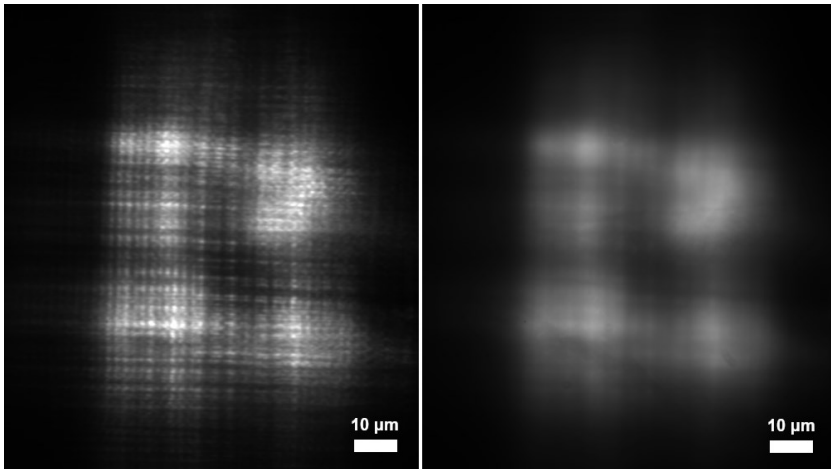


Figure 5-8: Measured intensity distribution of the 1st condenser lens of layout 1482_00_A0, for the 4th objective lens of layout 1278_00_A0; without (left) and with a diffuser (right); the scale shows the dimensions in the sample plane

This is due to two different factors. First – as for the first iteration of the optics – the absorption of objective lens and condenser have been neglected. This was necessary to limit the computation time and to be able to get a better understanding of what exactly happens in such a complex system as the combination of illumination prism lens and CRL objective.

The second – and more significant factor– is the incident beam intensity distribution itself. The beam cross section both in horizontal and vertical direction – assuming an undulator source – has a slightly diverging behaviour; additionally, the vertical intensity distribution follows a Gaussian distribution. This means that most photons are concentrated on the optical axis, while as the distance from the optical axis increases, fewer and fewer photons enter the aperture of the optics. As it has been explained earlier [37], the more diffuse the illumination on the sample, the better image quality can be expected. But only if the rays are accepted by the objective lens and will contribute to the captured image. This, and the absorption conditions of the objective lens, optimally would require a beam profile providing most intensity furthest from the optical axis and decreasing intensity towards the optical

axis. In the outlook of this chapter a solution will be introduced that is expected to solve this problem.

Despite the challenging circumstances and far from optimal illumination optics, an image of a test pattern was acquired as shown in Figure 5-9.

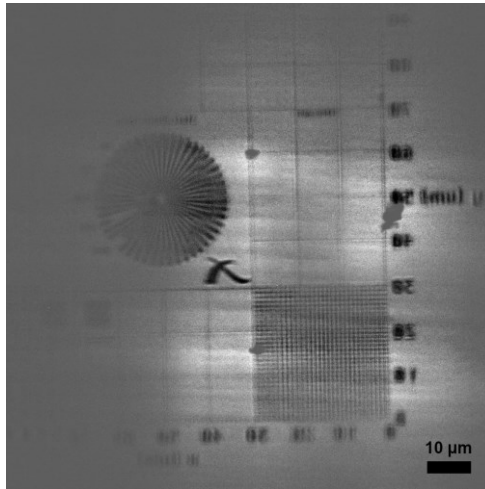


Figure 5-9: Microscope image of a test pattern using the first illumination optics in combination with a thick point focus CRL; the scale shows the dimensions in the sample plane

5.5 Summary prism condensers

It has been demonstrated that an adapted X-ray prism lens condenser can be successfully fabricated for thick CRL X-ray objectives.

Whereas the stray light was considered as a disadvantage on the end of chapter 4, introduced by the supporting planes, in this application this phenomenon leads to a more homogeneous more diffuse illumination.

First and most obviously, for a second set of optics it would be a major advantage to take into account the absorption properties of the objective lens and the condenser lens.

Further, as it has been shown, that the incident beam intensity profile of a typical synchrotron source is disadvantageous for an optimal illumination as the most intense part of the beam is in the very middle of it. Building a condenser out of two separate prism optics, arranged one behind the other, could solve this problem. The first part of the optics should divert the beam in the way, that the most intense parts would hit the outermost part of the second prism optics. In this way, the second optics could optimally redistribute the intensity towards the sample plane.

6 Optimizing synchrotron source illumination for full field imaging

In the case of material science as well as in biology and medical imaging techniques like X-ray tomography are used at high brilliance synchrotron sources [39], [41]-[47]. For these sources, the beam is usually much narrower in the vertical direction than in the horizontal direction. Additionally, the intensity distribution of such a source is approximately Gaussian in vertical direction with the full width half maximum (FWHM) size in the range of about a millimetre, at around 35 m from the source at a typical beamline [48]. These characteristics strongly limit the maximum possible sample size [49], [50].

6.1 Aim and main challenges

Using enlarged shadow projection [51] or simply stitching several acquired images [50] one can try to overcome these limitations. Drawbacks are possible image artefacts and the additional time needed for the acquisition of the multiple height scans and the more complex image reconstruction. In the case of biological samples, the higher radiation dose in the overlapping image areas due to the multiple scans generates damage in the sample, thus filters might have to be introduced to reduce the flux penetrating the sample. Especially for in-situ and operando experiments scanning of the sample is not applicable because of the obvious limitations in time resolution. The possibility of applying cone beam projection is given here as well; however, this leads to using additional optics to form a virtual source. In this case, along the reconstruction, the parallel beam approach cannot be applied and the alignment of these optics often is time consuming.

The Gaussian intensity profile of the beam results in location-dependent differences in the signal-to-noise ratio between the more illuminated regions in the centre and the less illuminated regions toward the edges of each scan. Based on these reasons a more homogeneous intensity distribution would be highly preferable and beneficial in full field shadow projection imaging applications. The main aim of this project was to develop such an optics that is capable of successfully transforming the Gaussian intensity distribution of the incident beam into a close to flat-top distribution with high homogeneity.

6.2 Design considerations

To achieve the above goal, it was necessary to design optics that would allow the incident intensity to be redistributed from areas of high intensity near the optical axis to broader areas of lower intensity and to be concentrated from parts of the Gaussian tails into smaller areas, as shown in Figure 6-1.

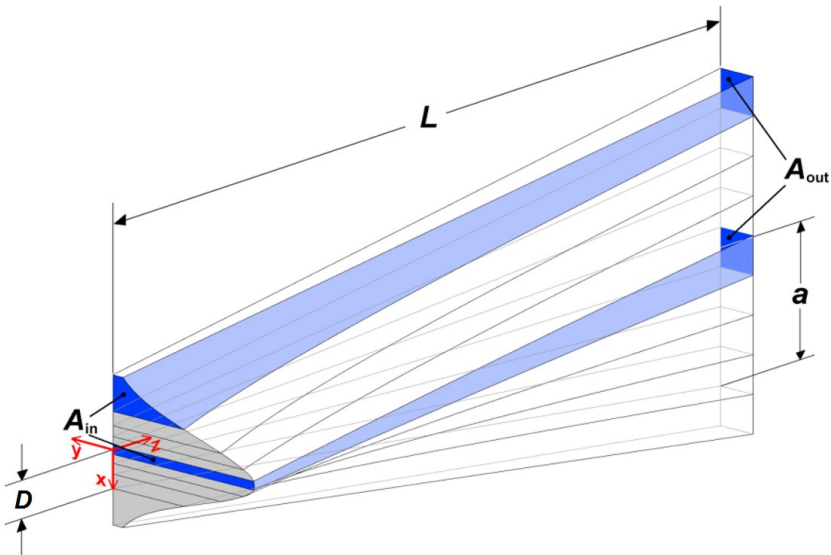


Figure 6-1: Incident Gaussian beam intensity (left) transformed into desired flat-top profile (right) with L the working distance of the optics; D is a defined width and A_{in} is a partial area in the Gaussian beam intensity profile, which relate to a and A_{out} in the flat-top intensity distribution

The general requirement is that, the optics must have a focal length that varies across the entrance aperture. As the incident beam has a narrower size than the desired one, this focal distance has to be negative, so the optics is overall defocusing. Close to the optical axis, the optics must have a short focal length, which increases within the aperture with increasing distance from the optical axis. All along the description, x - and y -directions are perpendicular to the optical axis, which is defined as z -direction. In the design procedure the optics will be considered lossless.

The optics should expand the beam in vertical direction (x -direction) and the intensity distribution of the incident beam can be described as

$$I_{(x)} = I_0 e^{-kx^2} \quad (6.1)$$

as a function of x -distance in vertical direction, considering k as a constant and I_0 as the intensity in the centre of the beam. Limiting the area of interest to the $x = c$ and $x = d$ boundaries, the integrated intensity looks like

$$\int_c^d I_{(x)} dx = \frac{I_0}{2} \sqrt{\frac{\pi}{k}} [\operatorname{erf}(\sqrt{k}d) - \operatorname{erf}(\sqrt{k}c)] \quad (6.2)$$

the sum of intensity, defining the total beam width D is

$$I_{\text{total}} = \int_{-\frac{D}{2}}^{\frac{D}{2}} I_{(x)} dx = I_0 \sqrt{\frac{\pi}{k}} \operatorname{erf}\left(\sqrt{k} \frac{D}{2}\right) \quad (6.3)$$

Defining the desired size of the illuminated area in vertical direction as B , the exiting flat-top intensity I_{top} can be written as

$$I_{\text{top}} = \frac{I_{\text{total}}}{B} = \frac{I_0}{B} \sqrt{\frac{\pi}{k}} \operatorname{erf}\left(\sqrt{k} \frac{D}{2}\right) \quad (6.4)$$

A ray entering the lens in distance d along the x -direction, has to be redirected to a point in the distance a from the optical axis, so the integral of the intensities on both sides of the optics are equal for all d (see Figure 6-1). The

focal length for every single ray in this distance d is calculated from the intensity distribution $I_{(d)}$ of the incoming beam.

$$\int_0^d I_{(x)} dx = \frac{I_0}{2} \sqrt{\frac{\pi}{k}} \operatorname{erf}(\sqrt{k}d) = a * I_{\text{top}} \quad (6.5)$$

Distance a can be calculated by including the upper last two equations:

$$a_{(d)} = \frac{B \operatorname{erf}(\sqrt{k}d)}{2 \operatorname{erf}\left(\sqrt{k}\frac{D}{2}\right)} \quad (6.6)$$

With the distance between optics and the imaging plane defined as L and considering the length of the optics negligible measured to its distance to the sample plane, furthermore assuming the incoming rays to be parallel to the optical axis, using the intercept theorem the focal length $f_{(d)}$ is given by

$$f_{(d)} = \frac{L * d}{a_{(d)} - d} \quad (6.7)$$

The resulting local focal length $f_{(d)}$ can be seen in Figure 6-2 as function of the distance from the optical axis.

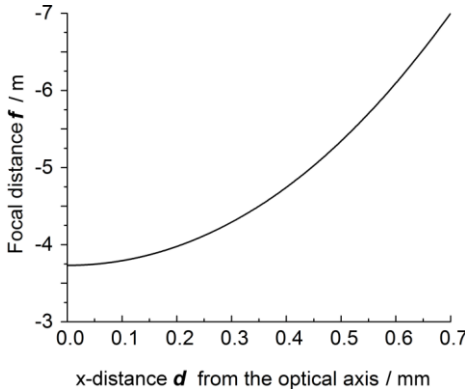


Figure 6-2: Local focal length f across the lenses' aperture ($D = 0.8$ mm, $L = 30$ m)

As a result, the shape of the required refracting surface can be calculated. As basis, the description of the lens geometry of a biconcave compound refractive lens (CRL) can be used:

$$R = 2 \cdot f \cdot \delta \cdot N \quad (6.8)$$

where R is the minimal radius of curvature in the apex of the parabola, δ is the decrement of refractive index of the lens material, N is the number of lens elements and f is the focal distance of the lens [52]. This equation gives a good approximation when the lens length is negligible with respect to the focal distance [53]. This approximation is applicable in this case as well, as the optics has the length in the centimetre range, although the distance to the source as well as to the detector or sample are in the tens of metres range. The shape of a normal CRL surface can be described as

$$z = \frac{x^2}{2R} \quad (6.9)$$

In the case of the beam shaper, the radius of curvature R is a function of the distance along x -direction. As this desired surface cannot be described in a closed analytical form, it has been numerically calculated starting at the optical axis, where the tangent of the surface is perpendicular to the axis.

The resulting element (see Figure 6-3 (a)) absorbing too much radiation, as the bulk itself does not contribute to the optical function of the lens. Considering the fact that the optics serves only illumination purposes, converting these elements to a sort of Fresnel-lenses [54] is an obvious solution.

Because of the limitations in fabrication, the corner angle β (see Figure 6-3 (b)) has a lower boundary of 20° . Therefore, the number of elements N is chosen to fulfil this requirement under every circumstances.

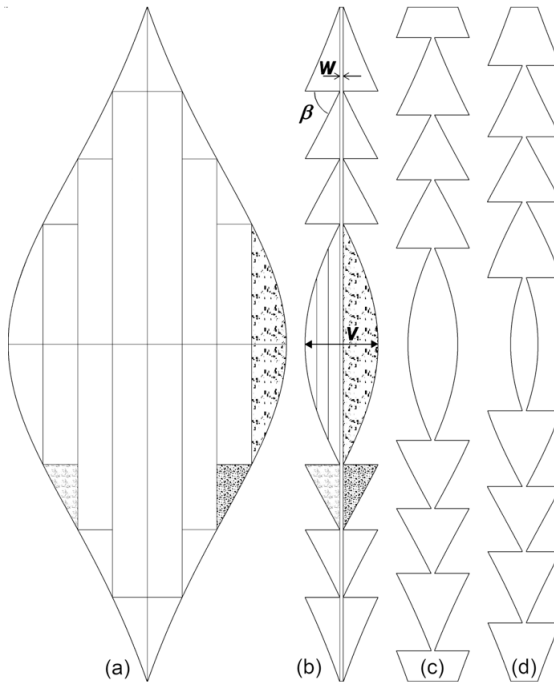


Figure 6-3: The underlying principle shape of a single element of these beam shaping optics divided in eight slices is shown in (a). The conversion of (a) into a Fresnel-element is indicated in (b), with a constant thickness w in the centre of the optics and the inner corner angle β . The structures in (c) and (d) are Fresnel-elements with modified diameter of the innermost zone forming a block structure together with (a). The group of elements (b), (c), (d) forms the smallest building block (zone) for the macroscopic lens to homogenize the projected thickness.

Following the basic principle of Fresnel-lenses, rectangular blocks are removed from every lens element. M - in the case of the example shown in Figure 6-3 (a) equals eight - is the number of parts or slices every element is being divided to. Removing the rectangular blocks and shifting the coherent parts together the lens is realized. Thus, the lower limit of amount of absorbing material is determined again by the limitations of fabrication and the absorption of the base material. The elements shown in Figure 6-3 (b) are still not optimal. If a lens would be realized in a way that these elements would be stacked after each other, the homogeneity of intensity would be reduced by up to 15 %, based on simulations. The obvious solution would be to further

increase the numbers of the slices and thus further reduce the steps between the Fresnel-elements. However, because of the fillets introduced by the fabrication process, is technically not feasible.

A different approach instead of using identical elements, is to vary them in shape to reduce the effect mentioned above. Forming K zones of a number of

$$P = \frac{N}{K} \quad (6.10)$$

different lens elements sliced in different ways. In the case explained in Figure 6-3 the Fresnel-elements (b) to (d) form such a zone. Simply the difference in the width of the innermost block leads to P different slices. v meaning the thickness of the innermost block of an original Fresnel-element is divided by P of different slices in one zone. The thickness of the innermost structure of P different lens elements is

$$\frac{mv}{P} \text{ with } m \in \mathbb{N} \cap m < P. \quad (6.11)$$

This results in elements varying in shape and a much more homogeneous, intensity distribution.

The optics is designed for the P05 imaging beamline operated by HZG at the storage ring at PETRA III (DESY, Hamburg, Germany) [55], [56]. The instrument, being optimized for in-situ experiments in particular is using an undulator source leading to a limited field of view. The beam characteristics are being 1.6 mm to 2 mm FWHM in vertical and around 7 mm FWHM in horizontal direction at sample position. This inherent property of undulator sources leads to a less than ideal situation for full field imaging. For many samples in cases of radiography and tomography, a larger FoV would be better [55].

6.3 Realization

Based on the method described above, a novel type of beam enlarging optics has been developed, with the following main design parameters:

- Photon energy: 24 keV
- Source distance: 60 m
- Working distance: 30 m
- Physical entrance aperture: 1.4 mm

Part of the intermediate mask of the resulting layout can be seen in Figure 6-4, as a SEM image. The lens contains $N=20$ elements, in zones of $P=5$ different slices, each with $M-1=15$ segments. The minimum thickness of the elements has been defined as $w=6\ \mu\text{m}$, the air gap between the lens elements has been chosen to be $150\ \mu\text{m}$. The technically achievable minimum edge rounding radius has been assumed to be $0.5\ \mu\text{m}$.

Three sets of optics have been designed for three different photon energies of 10 keV, 17 keV and 24 keV. This method of lens shape creation is highly dependent on the incident beam intensity distribution. Three different sigma values have been assumed for the Gaussian intensity distribution of the incoming beam at the entrance aperture of the optics: $170\ \mu\text{m}$, $340\ \mu\text{m}$ and $540\ \mu\text{m}$. For each of these sigma values one lens was designed, thus in total nine lenses. The design parameters have been determined based on the light source data provided by the beamline operators. More details are included in the data sheet of layout 1489_00_A0 in appendix A.

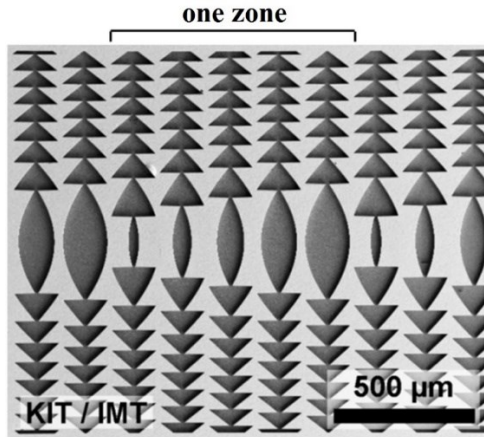


Figure 6-4: SEM image of a part of an intermediate X-ray absorber mask for beam shaping optics fabrication (Layout 1489_00_A0, lens no.1)

There are ideas, to reduce the dependency on the sources' intensity distribution and thus develop optics to be universally applicable. Similarly to the microscope condenser application described in chapter 5, the beam can be divided into smaller portions redirected by prisms and μ CRLs, as it was similarly introduced before as “new concept” in chapter 5.2. In this way, the resulting intensity distribution can be described as a superposition of multiple smaller beamlets dealt with separately, thus the dependency on the source can be eliminated. Furthermore, such optics would have a significantly higher transmission for the same application compared to CRLs.

The idea is basically the same as it has been described in chapter 5.2. Prisms redirect the beamlets towards a focal point on the optical axis, combined with biconvex μ CRLs, spreading the beamlets to the overall desired beam width. As the beam is effectively an overlap of these beamlets, the intensity distribution would be necessarily homogeneous and constant, as it is required.

As it can be seen in Figure 6-5, every row has an equal number of μ CRLs, leading to a constant beam width and constant intensity. An increasing number of prisms with increasing distance from the optical axis is required. Using this concept, the designer of the optics can tailor the beam intensity distribu-

tion, as the application requires it, independently of the incident beam properties.

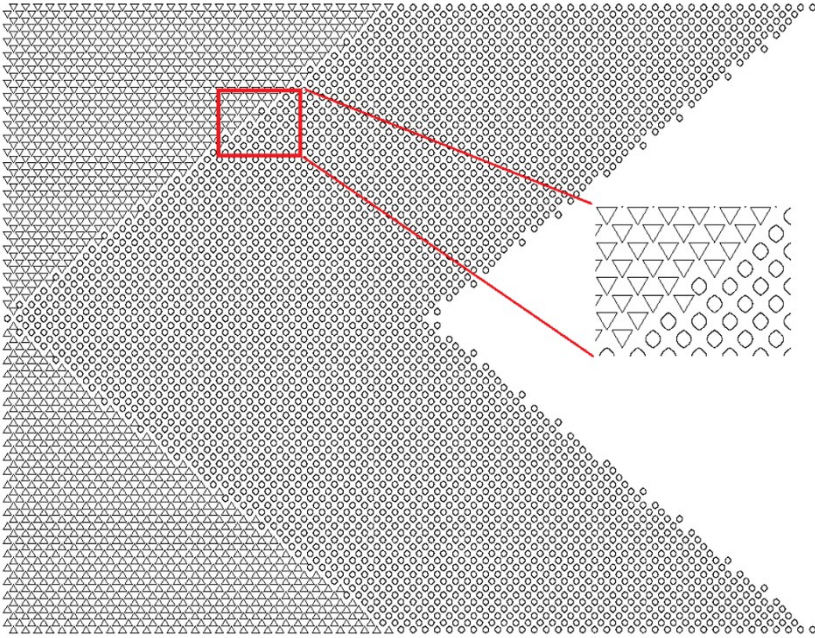


Figure 6-5: Novel concept of a universal beam shaper

6.4 Simulation and experimental results

The first set of lenses has been fabricated in ca. 800 μm high resist, as a limitation of LIGA fabrication process at the time. For the experiment two halve lenses have been mounted onto separate holders and turned face-to-face towards to each other, to achieve the requested 1.6 mm aperture in horizontal direction. This way it has been proven that the optics can be stacked for applications requiring larger apertures than feasible with the actual standard

lithography process. Figure 6-6 shows a photograph of the diced lens plates mounted on the lens carrier. Two sets like this have been prepared.

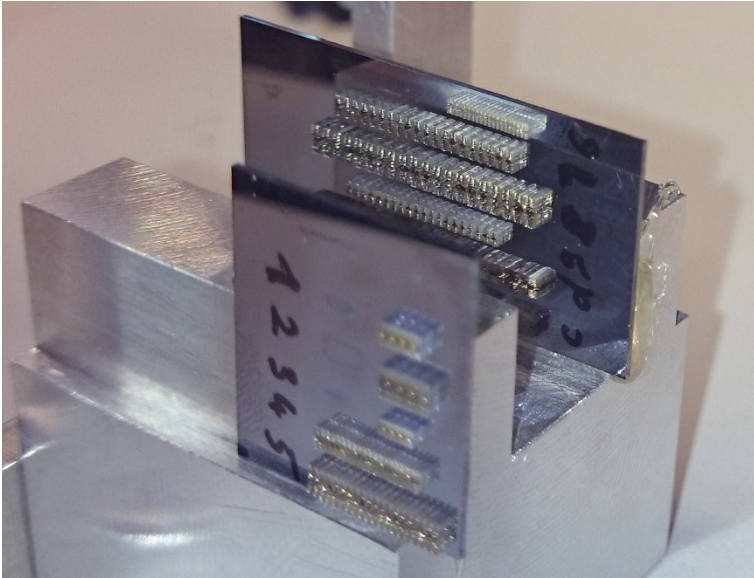


Figure 6-6: Lens halves mounted on the lens carrier, in the control hutch of PETRA III / P05

The main goal of the optical characterization – that took place at the imaging beamline PETRA III / P05 – was to determine the beam enlargement capabilities and the beam intensity homogeneity at detector position.

The upper part of figure 6-7 has been acquired with 5x magnification and $2.48 \mu\text{m}$ virtual pixel size in the scintillator plane. The detector image shows the presence of the beam shaper optics; resulting in a field of view widened in vertical direction to $5.6 \text{ mm} \times 1.6 \text{ mm}$ (only two $800 \mu\text{m}$ beam shapers were stacked). On both sides of the expanded beam, the original, nearly Gaussian beam can be seen with 1.35 mm FWHM. The two black areas between the enlarged and original beam parts are due to the lens substrates on both sides.

The lower part of Figure 6-7 shows the beam enlarging result in the form of graphs. The narrower, and higher peaking plot is the original, nearly Gaussian incident beam (blue). The wider plot with lower intensity is the flat-top like intensity distribution realized by the optics (red).

The intensity profile is not perfectly flat, but the standard deviation of the shaped beam profile is only about 17 % of the average intensity. A slight asymmetry is present in the overall intensity profile thanks to the not perfectly Gaussian shaped incident beam.

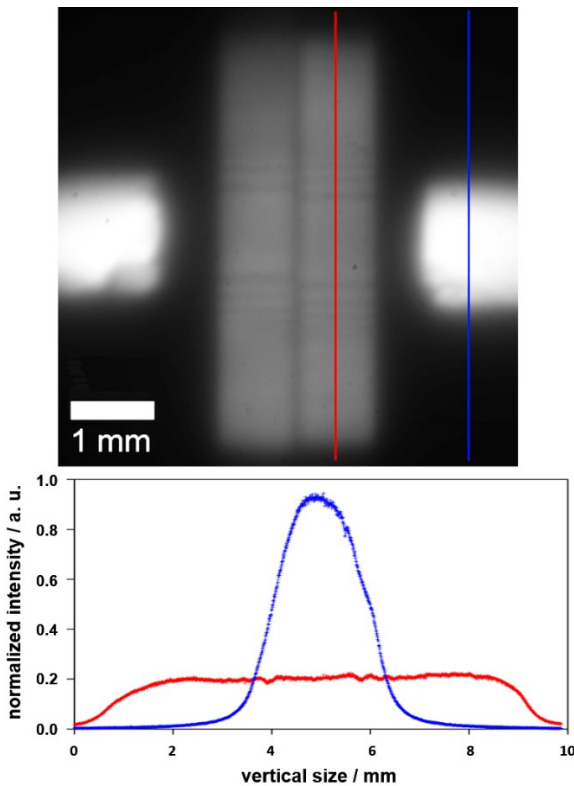


Figure 6-7: Result of the beam shaper profile measurement at PETRA III / P05 with the original beam intensity (blue line) and the more flat-top like beam intensity after the optics (red line). Upper: detector image, lower: result in the form of graphs.

For the measurements of the optics, it has been placed only 21 m away from the sample, as a result of temporary beam line restrictions. Therefore, the measured height is only 5.6 mm instead of originally planned 7 mm. The distance between source and optics was 65 m. The sample to detector distance was 15 mm. As this distance is small compared to the distance optics to sample, there is no need of the use of a cone beam reconstruction algorithm in the image reconstruction. The principle sketch of the experimental setup can be seen in Figure 6-8.

The calculated efficiency of the optics is 83 %, being the ratio of the original incident and enlarged integrated intensity. The measured efficiency was only 63 %. The difference is most probably a result of a slight misalignment of the optics with respect to the incident beam and a small part of rays scattered off rounded edges.

As a practical test, to verify the performance of the optics, a 3 mm long sea urchin spine has been chosen as a test sample for a CT measurement. The experiment has been carried out at a photon energy of 24 keV. The X-rays have been converted to visible light by using a CdWO_4 scintillation screen, and a tenfold visible light magnification resulting in an effective pixel size of $1.25 \mu\text{m}$. The overall line and space resolution achieved was $3.9 \mu\text{m}$.

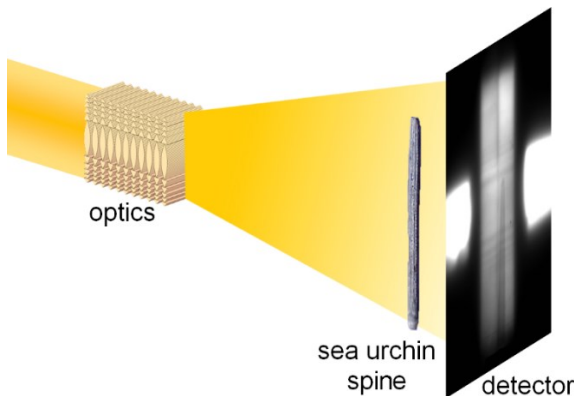


Figure 6-8: Experimental setup of the CT measurement to investigate a sea urchin spine using to validate the performance of the presented beam shaping optics

Using the standard CT acquisition scheme of the P05 micro tomography beamline, we did not face any negative influence of the optics on the image quality. After flat-field correction – as it is shown in Figure 6-9 (a) – no deviation compared to the stacked-scan can be noticed, neither in the background, nor in the foreground. The reconstructed volume shows no deviations or errors; no blur or artefacts can be noticed in any relation to the optics. In addition, the image resolution turned out to be the same with or without applying the optics. The histogram of the reconstructed slices shows only two distinct peaks: one for air and one for the sample, further verifying the quality of the optics.

In Figure 6-9 (b)-(d) can be seen a reconstructed slice of the sea urchin spine, clearly visualizing the porous matrix in the centre column of the sample.

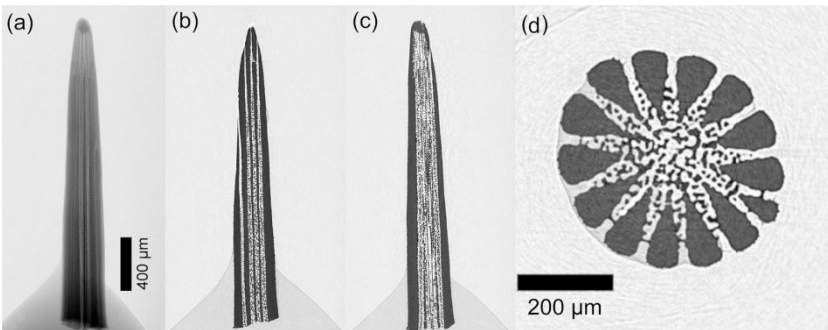


Figure 6-9: Tomography of a sea urchin spine to validate the performance of the presented beam shaping optics; absorption image (a) and reconstructed tomographic slices (b) to (d)

This project and its presentation has been honoured with the “*Best Poster of XRM2016*” award on the International Conference on X-ray Microscopy (XRM2016), Oxford, UK.

As it has been explained earlier, the first version of lens design – although fulfilling the desired aims – has major drawbacks like extreme dependency on the source characteristics and relatively high overall absorption. In short, the present optics has to be customized for each individual setup.

As explained at the end of chapter 6.3, there is a promising new concept to make the optics way more transparent and universal. In the following, some simulation results prove the benefits of this new design.

The universality of such lens has been considered above from the aspect of use and design as well. Although – as it is shown in Figure 6-10 – there are some interesting differences worth to be mentioned.

First, the difference in homogeneity is superior to the version that has been fabricated and characterised, as well as the transmission, increasing from 71 % to 86 %. Additionally, the physical length of the lens shrinks down to roughly 1/3 of the original. One would expect a greater increase in transmission based on the change of length, but most of the difference in length is due to the lens elements standing closer together. The lenses below are certainly different in behaviour, as the second version is widening the beam up to 7.4 mm FWHM, as the first version is responsible only for a smaller effect, resulting in 6.7 mm FWHM.

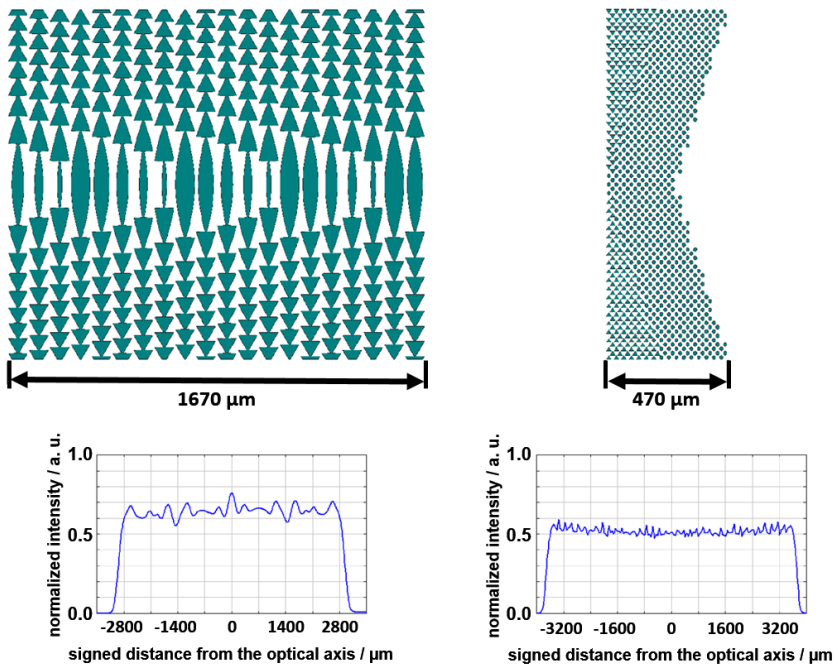


Figure 6-10: First kinoform like version of the beam shaper design (left) versus the successor XPL with biconcave μ CRLs (right), with simulation results below

6.5 Summary beam widening lenses

The presented optics successfully eliminate the vertical beam size limitation at high brilliance synchrotron sources, opening up new application areas for shadow projection imaging, especially on the field of in-situ and operando experiments. Additionally, the optics converts the standard Gaussian like beam profile into an advantageous more homogeneous intensity distribution. This flat-top like profile with a more uniform illumination increases the signal-to-noise ratio at the upper and lower border of the field of view and therefore the image quality.

Fourth generation synchrotron sources (diffraction limited storage rings) aim to further decrease the beam size, even further in horizontal direction. Needless to say, how beneficial it will be to introduce such optics to keep the possibility of micro tomography and similar techniques at these beamlines.

7 Conclusion and outlook

Within this work, two main challenges were addressed, one is being stabilizing the structure of X-ray prism lenses (XPLs) and the second is developing novel illumination optics, for full-field imaging, focusing and condensers for full-field microscopy illumination.

As a first example throughout chapter 5, a focusing optics has been realised with better transmittance of up to 54 % and – depending the application – up to 10 to 40 times wider entrance aperture than conventional compound refractive lenses. To achieve this, prisms have been aligned in rows together with equal size CRL elements to achieve a significantly smaller focal spot size than ever before using XPLs. The method of stabilizing high aspect ratio prisms with edge length of 20 μm and heights up to 1.6 mm by tilted supporting planes was demonstrated successfully here for the first time. Overcoming the limited aspect ratio of the prism columns made it possible to fabricate XPLs with apertures as wide as 1.6 mm for two-dimensional optics with low absorption.

In chapter 6, a first approach of an illumination optics for an X-ray microscope has been presented. The concept behind the design of the condenser is more or less the same as it was for the focusing prism lenses with two differences: First, the beamlets exiting a prism row point to a certain point of the entrance aperture of the objective lens instead of the focal point on the optical axis. Second, double-convex elements have been used to diverge the beamlets exiting each prism row to assure the desired beam distribution. In this way it is possible to concentrate as many photons as possible on the sample, covering the acceptance requirements of the objective lens.

A first version of such a condenser optics was tested in the beam. It has been proven that a adapted condenser optics can be fabricated for thick CRL objectives. The field of view of about 50 μm x 50 μm was as planned, but the homogeneity needs further improvement. Stray light is normally considered

as a disadvantage in optics. In the condenser lens, scattering produced in the intersection areas of prisms with the supporting planes, can lead to a more homogeneous, diffuse illumination, although at the expense of some efficiency.

Throughout the last main chapter of the work, a novel refractive optical element has been introduced, supporting full-field imaging at high brilliance synchrotron sources. The main point of this optics is to widen the highly asymmetric beam cross section of about 2 mm to a more homogeneous, more square-like shape with nearly 6 mm beam height at the sample position. This goal was achieved by rearrangement of the beam along the whole aperture. In short, an individual lens contour with a varying focal distance has been created. To avoid high absorption near the optical axis, the optics were designed as a kinoform lens.

The presented optics successfully eliminate the vertical size limitation at synchrotron sources, opening up new application areas for shadow projection imaging, especially in the field of in-situ and operando experiments. Additionally, it creates a significantly more advantageous situation, providing a more homogeneous intensity distribution than the standard Gaussian like. This flat-top like profile with a more uniform illumination increases the signal-to-noise ratio in the upper and lower part of the field of view and therefore the image quality.

In the outlook for future development, the individual optics must be treated individually. To further improve the condensers, the significant amount of stray light generated by the supporting planes tilted around an axis perpendicular to the optical axis should be decreased. A mayor development option could be to optimise the orientation as well as the thickness of these planes. Tilted supporting planes parallel to the optical axis would reduce the amount of stray light significantly. Of course, the planes would absorb all rays hitting the front side of such supporting planes.

Further development options are to overcome the limitations related to the integer number of prisms and μ CRLs. The radius of the μ CRLs as well as the angle of the prisms can be fine-tuned in a two-stage computation. After in the

first pass the necessary number of elements is established, based on this value the mentioned parameters can be tailored in a manner that they would fit perfectly to the requested working distance of elements. For a second, improved optics layout it would be a huge advantage to take into account the absorption properties of the objective lens and the condenser.

The intensity profile of the incident beam from a synchrotron source is unfavourable for optimal illumination, due to absorption most of the intensity is needed in the edge regions of the condenser for proper illumination. Using a two-stage condenser, this problem could be solved. A first, beam-widening part of the optics should divert the beam in the way that the most intense parts would hit the outermost part of the second stages' aperture, and the intensity would be progressively decreasing, towards the optical axis. The second stage basically would act as it has been described above.

To further improve the beam widening optics, a second version of these lenses should be fabricated and tested. The only "disadvantage" of the new design is the required extreme computational power, especially for the simulation of these optics. The required ultra-high aspect ratios could be realized using supporting planes as in other XPLs. If the performance of the optics could be demonstrated in practice, then new and universal optics could be offered to the scientific community, as a new tool for full field imaging, at high brilliance synchrotron sources.

Fourth generation synchrotron sources (diffraction limited storage rings) aim to further decrease the beam size, also in horizontal direction. Needless to say, how beneficial it will be to introduce such optics to keep the possibility of micro tomography at these beamlines.

The main goals of this research have been successfully addressed and achieved; furthermore, possible new ways for the development of X-ray optics have been outlined.

Appendix

A Lens layout parameters

Lens layout 1351_00_A0

Layout 1351_00_A0 contains twelve prism condenser lenses for use at the synchrotron source SPring-8, beamline BL43LXU. All prisms are 60°-prisms, partly combined with μ CRLs.

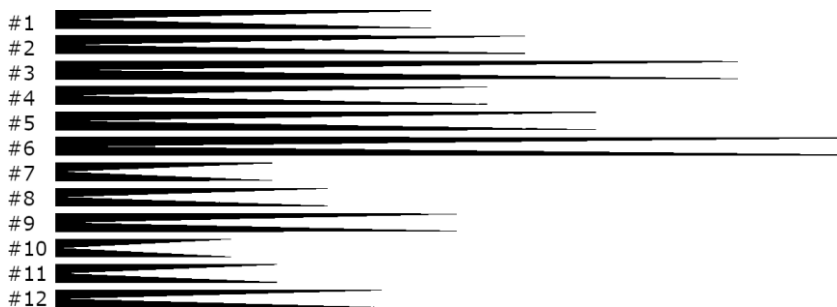


Figure A-1: Image of layout 1351_00_A0

Table A-1: Parameter summary of layout parameters:

Lens number	Prism edge length [μ m]	Combined with μ CRLs	Photon energy [keV]	Note
#1	20	yes	15.815	for pre-focus 6 m
#2	20	yes	17.764	for pre-focus 6 m
#3	20	yes	21.747	for pre-focus 6 m
#4	20	yes	15.815	for pre-focus 7 m
#5	20	yes	17.764	for pre-focus 7 m
#6	20	yes	21.747	for pre-focus 7 m
#7	10	no	15.815	for pre-focus 7 m
#8	10	no	17.764	for pre-focus 7 m
#9	10	no	21.747	for pre-focus 7 m
#10	8	no	15.815	for pre-focus 7 m
#11	8	no	17.764	for pre-focus 7 m
#12	8	no	21.747	for pre-focus 7 m

Lens layout 1574_00_A0

Layout 1574_00_A0 contains ten prism condenser lenses for use at the synchrotron source SPring-8, beamline BL43LXU. All prisms are 60° -prisms, combined with μ CRLs.

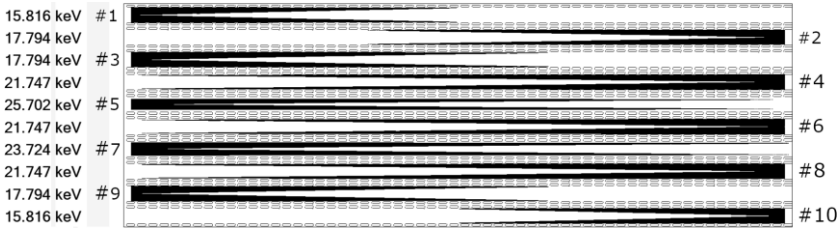


Figure A-2: Image of layout 1574_00_A0

Table A-2: Parameter summary of layout parameters:

Lens number	Prism edge length [μm]	Photon energy [keV]	Aperture [mm]
#1	18	15.816	1.3
#2	18	17.794	1.3
#3	18	17.794	1.3
#4	18	21.247	1.3
#5	18	25.702	0.92
#6	18	21.747	1.3
#7	18	23.724	1.02
#8	18	21.747	1.3
#9	18	17.794	1.3
#10	18	15.816	1.3

Data sheet of layout 1482_00_A0

Layout 1482_00_A0 contains nine times two half-prism condenser lenses, thus giving nine XPL condensers. All prisms are 60° -prisms.

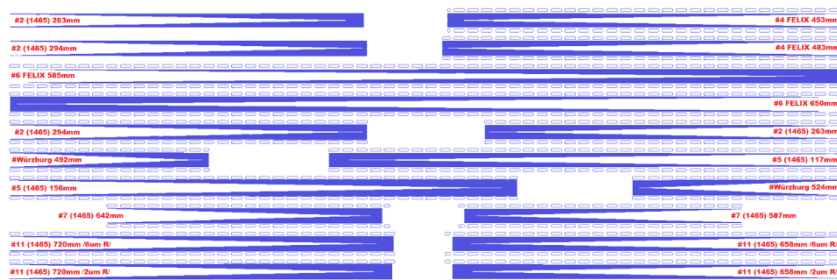


Figure A-3: Image of layout 1482_00_A0

Table A-3: Parameter summary of layout 1482_00_A0:

Lens name	Working distance from entrance aperture [mm]	Aperture [μm]	Photon energy [keV]	Lens length [mm]	Distance objective to sample [mm]	Prism edge length [μm]	Field of view [μm]
#2A for layout 1465, with/without blocks	294	1.1	13	<26	60	20	150
#2B for layout 1465, with/without blocks	263	1.0					
#4A for layout 1278	483	1.06	17.4	<29	77	20	100
#4B for layout 1278	453	1.0					
#5A for layout 1465	156	1.2	17.4	<37	80	10	400
#5B for layout 1465	117	1.0					
#6A for layout 1278	650	1.1	30	<59	65	18	100
#6B for layout 1278	585	1.0					
#Würzburg_A for layout 1465	524	1.08	9.3	<15	70	10	80
#Würzburg_B for layout 1465	492	1.02					
#7A for layout 1465	642	1.08	24	<20	150	10	150
#7B for layout 1465	587	1.0					
#11A, $R_{\mu\text{CRL}}=2\ \mu\text{m}$, for layout 1465	720	1.08	24	<28	150	10	150
#11B, $R_{\mu\text{CRL}}=2\ \mu\text{m}$, for layout 1465	658	1.0					
#11A, $R_{\mu\text{CRL}}=6\ \mu\text{m}$, for layout 1465	720	1.08	24	<28	150	10	150
#11B, $R_{\mu\text{CRL}}=6\ \mu\text{m}$, for layout 1465	658	1.0					

Data sheet of layout 1489_00_A0

Layout 1489_00_A0 contains thirteen different beam-widening lenses, some of them multiple times. Each lens has five zones of different slices, a source to optics distance of 60 m and an optics to sample distance of 30 m.

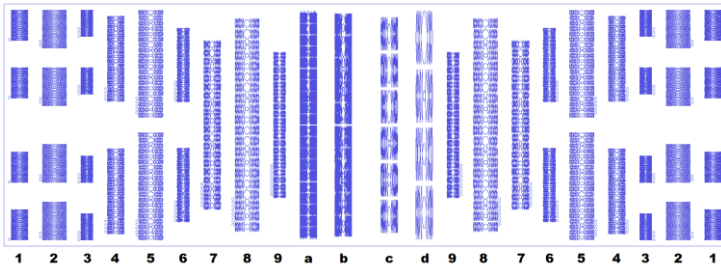


Figure A-4: Image of layout 1489_00_A0

Table A-4: Parameter summary of layout 1489_00_A0:

Lens no.	Photon energy [keV]	σ at entrance aperture [μm]	Aperture [mm]	Number of segments []	Notes
#1	10	340	1.4	15	4x the same lens
#2	10	540	2.0	15	4x the same lens
#3	10	170	1.0	15	4x the same lens
#4	17	340	1.4	15	2x the same lens
#5	17	540	2.0	15	2x the same lens
#6	17	170	1.0	15	2x the same lens
#7	24	340	1.4	15	one complete lens
#8	24	540	2.0	15	one complete lens
#9	24	170	1.0	15	one complete lens
#a	50	340	1.4	51	one complete lens
#b	50	340	1.4	25	part of a lens
#c	50	340	1.4	15	part of a lens
#d	50	340	1.4	9	part of a lens

B Calculation software

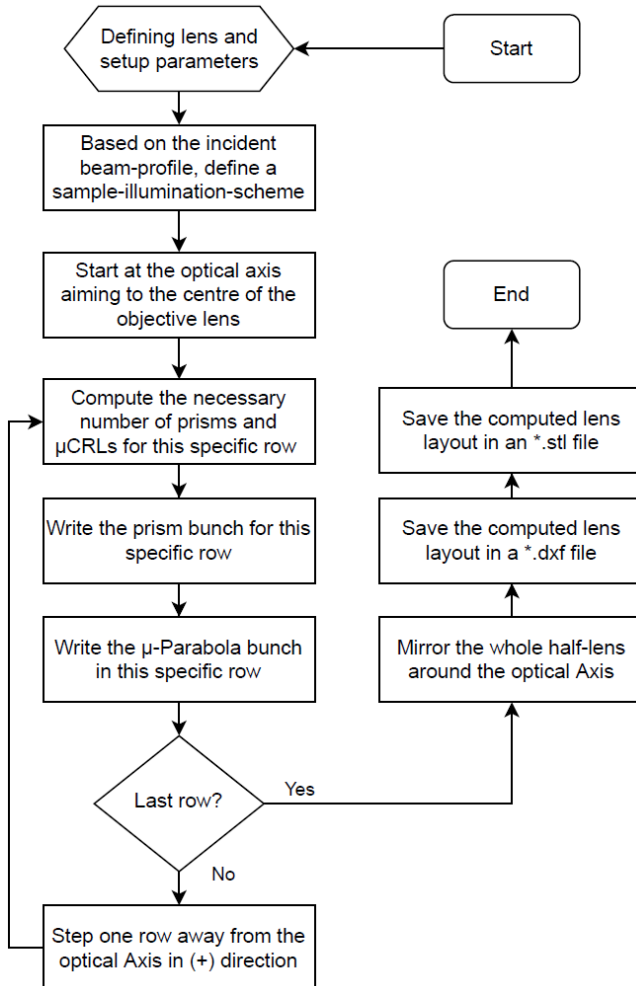


Figure B-1: Flow chart of software to calculate the layout for condenser optics

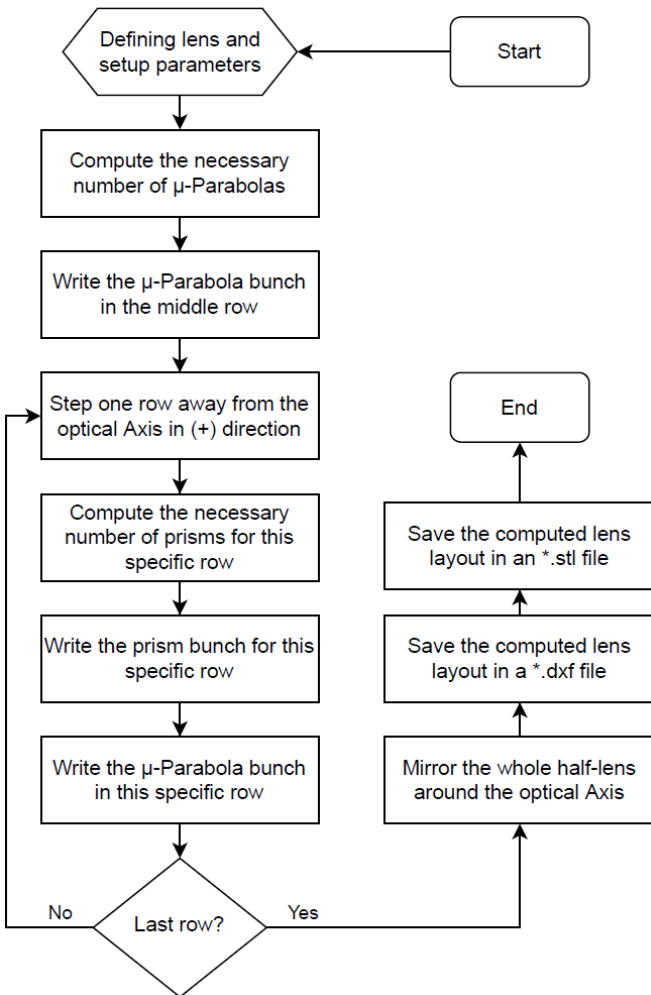


Figure B-2: Flow chart of software to calculate the layout for focusing optics

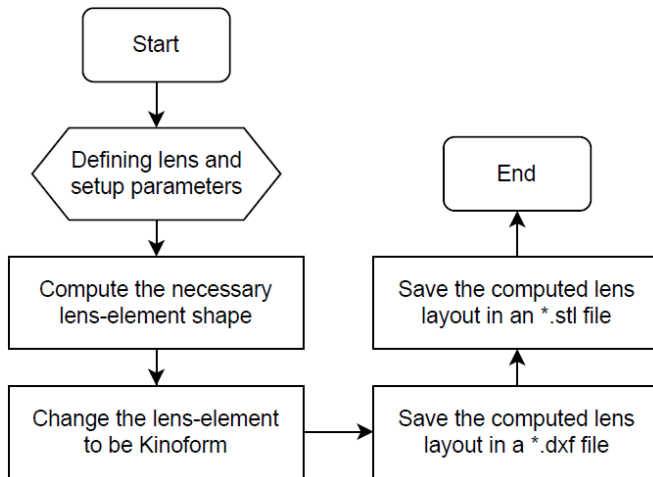


Figure B-3: Flow chart of software to calculate the layout for beam shaping optics

C List of own publications

Peer-reviewed publication list (in chronological order)

E. Kornemann, T. Zhou, O. Márkus, A. Opolka, T. U. Schüllli, J. Mohr and A. Last, “X-ray zoom lens allowing for energy scans in X-ray microscopy,” *Opt. Express* 27, 185-195 (2019), doi: 10.1364/OE.27.000185

E. Kornemann, O. Márkus, A. Opolka, K. Sawhney, A. Cecilia, M. Hurst, T. Baumbach, A. Last and J. Mohr, “Optical Characterization of an X-ray Zoom Lens,” *Microscopy and Microanalysis* 24(S2), 268-269 (2018), doi: 10.1017/S1431927618013685

O. Márkus, I. Greving, E. Kornemann, M. Storm, F. Beckmann, J. Mohr and A. Last, “Optimizing illumination for full field imaging at high brilliance hard X-ray synchrotron sources,” *Opt. Express* 26, 30435-30443 (2018), doi: 10.1364/OE.26.030435

E. Kornemann, O. Márkus, A. Opolka, T. Zhou, I. Greving, M. Storm, C. Krywka, A. Last and J. Mohr, “Miniaturized compound refractive X-ray zoom lens,” *Opt. Express* 25, 22455-22466 (2017), doi: 10.1364/OE.25.022455

Chr. Krywka, A. Last, F. Marschall, O. Márkus, S. Georgi, M. Müller and J. Mohr, “Polymer compound refractive lenses for hard X-ray nanofocusing,” *AIP conference proceedings* 1764, 020001 (2016), doi: 10.1063/1.4961129

F. Koch, F. Marschall, J. Meiser, O. Márkus, A. Faisal, T. Schröter, P. Meyer, D. Kunka, A. Last and J. Mohr, “Increasing the Aperture of X-ray Mosaic Lenses by Freeze Drying,” *Journal of Micromech. Microeng.* 25, 075015 (2015), doi: 10.1088/0960-1317/25/7/075015

A. Last, M. Börner, F. Marschall, P. Meyer, M. Simon, O. Márkus, S. Georgi and J. Mohr, “Auswirkungen von Reflexen an Seitenwänden von Goldabsorbern in der Röntgentiefenlithographie,” *Tagungsband Mikrosystemtechnik Kongress: MEMS, Mikroelektronik, Systeme*, 26.-28.10.2015, Karlsruhe, VDE, ISBN 978-3-8007-4100-7 (2015)

A. Last, O. Márkus, S. Georgi and J. Mohr, “Röntgenoptische Messung des Seitenwandwinkels direktlithografischer refraktiver Röntgenlinsen,” *Tagungsband Mikrosystemtechnik Kongress: MEMS, Mikroelektronik, Systeme*, 26.-28.10.2015, Karlsruhe, VDE, ISBN 978-3-8007-4100-7 (2015)

W. Jark, A. Last and O. Márkus, “High-speed photon energy tuning of x-rays with high duty cycle by use of Clessidra prism arrays,” *SPIE Proceedings* 8848, *Advances in X-Ray/EUV Optics and Components VIII*, 884806 (2013), doi: 10.1117/12.2023921

Conference Contributions (only as presenting author)

O. Márkus, S. Georgi, I. Greving, E. Kornemann, A. Last, J. Mohr and M. Ogurreck, “X-ray beam shaping by polymer lenses,” poster presentation, STN-day 2016, Karlsruhe, Deutschland

O. Márkus, S. Georgi, I. Greving, E. Kornemann, M. Ogurreck, F. Beckmann, A. Last and J. Mohr, “X-ray beam shaping by polymers,” poster presentation, XRM 2016, Oxford, UK (**best poster award**)

Patent

Ottó Márkus, Frieder Koch, “Photoresiststruktur und Verfahren zu ihrer Herstellung,” patent no. DE102015217201B3, 2017

References

- [1] E. J. Als-Nielsen and D. McMorrow, Elements of Modern X-ray Physics, 2nd Edition, Wiley, 2011.
- [2] H. Winick, Synchrotron radiation sources : a primer, Series on Synchrotron Radiation Techniques and Applications Vol.1, Singapore [u.a.] : World Scientific, 1995.
- [3] D. M. Mills, Third-generation hard x-ray synchrotron radiation sources : source properties, optics, and experimental techniques / ed. by Dennis M. Mills, New York : Wiley & Sons, 2002.
- [4] V. Saile, Synchrotron radiation and its applications in material science, Louisiana State University, Baton Rouge, 1988.
- [5] R. Bartolini, Electron beam dynamics in storage rings - Synchrotron radiation and its effect on electron dynamics, John Adams Institute, 2014.
- [6] J. T. Cremer, Neutron and X-ray microscopy, 1st edition, Amsterdam: Elsevier, 2012.
- [7] D. Vaughan, A. Thompson, J. Kirz, D. Attwood, E. Gullikson, M. Howells, K. Kim, J. Kortright, I. Lindau, P. Pianetta, A. Robinson, J. Underwood, G. Williams and H. Winick, X-ray Data Booklet, Lawrence Berkeley National Laboratory, University of California, 2001.
- [8] N. R. Pereira, E. M. Dufresne, R. Clarke und D. A. Arms, Parabolic lithium refractive optics for x rays, Review of Scientific Instruments 75, p. 37, 2004.

- [9] K. Young, A. Khounsary, A. N. Jansen, E. M. Dufresne and P. Nash, Fabrication and Performance of a Lithium X-Ray Lens, AIP Conference Proceedings 879, p. 989, 2007.
- [10] C. G. Schroer, M. Kuhlmann, B. Lengeler, T. F. Günzler, O. Kurapova, B. Benner, C. Rau, A. S. Simionovici, A. Snigirev and I. Snigireva, Beryllium parabolic refractive x-ray lenses, Proc. SPIE 4783, Design and Microfabrication of Novel X-Ray Optics, p. 10-19, 2002.
- [11] B. Nöhammer, C. David, H. Rothuizen, J. Hoszowska and A. Simionovici, Deep reactive ion etching of silicon and diamond for the fabrication of planar refractive hard x-ray lenses, Microelectron Eng. 67–68, p. 453–460, 2003.
- [12] A. Stein, K. Evans-Lutterodt, N. Bozovic and A. Taylor, Fabrication of silicon kinoform lenses for hard x-ray focusing by electron beam lithography and deep reactive ion etching, J. Vac. Sci. Technol. B 26 (1), p. 122-127, 2008.
- [13] V. Nazmov, E. Reznikova, A. Last, J. Mohr, V. Saile, M. DiMichiel and J. Göttert, Crossed planar x-ray lenses made from nickel for x-ray micro focusing and imaging applications, Nucl. Instrum. Methods Phys. Res. A 582(1), p. 120–122, 2007.
- [14] V. Nazmov, E. Reznikova, J. Mohr, A. Snigirev, I. Snigireva, S. Achenbach and V. Saile, Fabrication and preliminary testing of X-ray lenses in thick SU-8 resist layers, Microsystem Technologies 10, p. 716-721, 2004.
- [15] E. Reznikova, T. Weitkamp, V. Nazmov, M. Simon, A. Last and V. Saile, Transmission hard x-ray microscope with increased view field using planar refractive objectives and condensers made of SU-8 polymer, J. Phys.: Conf. Ser. 186, 012070, 2009.

-
- [16] X-Ray Interactions With Matter, The Center for X-Ray Optics Lawrence Berkeley National Laboratory. [Online]. Available: http://henke.lbl.gov/optical_constants/ [Accessed: 27 April 2021].
- [17] Overview over many kinds of X-ray optics, A. Last, [Online]. Available: <http://www.x-ray-optics.de/index.php/en/> [Accessed: 10 March 2021].
- [18] E. Kornemann, PhD-thesis: Entwicklung einer Röntgenzoomlinse, Karlsruhe Institute of Technology, KIT Scientific Publishing, 2018.
- [19] T. Tomie, X-ray lens, Patent Nr. US5594773A, 1994.
- [20] V. G. Kohn, I. Snigireva and A. Snigirev, Diffraction theory of imaging with X-ray compound refractive lens, *Optics Communications* 216, p. 247-260, 2003.
- [21] H. Chisholm, Hugh, "Lighthouse," *Encyclopædia Britannica*, 16 (11th ed.), Cambridge University Press, p. 627-651, 1911.
- [22] M. Simon, PhD-thesis: Röntgenlinsen mit großer Apertur, Karlsruhe Institute of Technology, KIT Scientific Publishing, 2010.
- [23] V. Nazmov, L. Shabel'nikov, F.-J. Pantenburg, J. Mohr, E. Reznikova, A. Snigirev, I. Snigireva, S. Kouznetsov and M. DiMichiel, Kinoform X-ray lens creation in polymer materials by deep X-ray lithography, *Nuclear Instruments and Methods in Physics Research* 217 (3), p. 409-416, 2004.
- [24] V. Nazmov, E. Reznikova, J. Mohr, A. Snigirev, I. Snigireva, S. Achenbach and V. Saile, Fabrication and preliminary testing of X-ray lenses in thick SU-8 resist layers, *Microsystem Technologies* 10, p. 716-721, 2004.

- [25] E. W. Becker, W. Ehrfeld, P. Hagmann, A. Maner, D. Muenchmeyer, Fabrication of microstructures with high aspect ratios and great structural heights by synchrotron radiation lithography, galvanofarming, and plastic moulding (LIGA process), *Microelectronic Engineering* 4, p. 35-56, 1986.
- [26] V. Saile, U. Wallrabe, O. Tabata, LIGA and its Applications, *Advanced Micro and Nanosystems* 7, Wiley-VCH Verlag, 2011.
- [27] M. Madou, *Fundamentals of Microfabrication: The Science of Miniaturization*, Second Edition, CRC Press, 2002.
- [28] A. L. Bogdanov and S. Peredkov, Use of SU-8 photoresist for very high aspect ratio X-ray lithography, *Microelectronic Engineering* 53, p. 493-496, 2000.
- [29] Chr. Krywka, A. Last, F. Marschall, O. Márkus, S. Georgi, M. Müller and J. Mohr, Polymer compound refractive lenses for hard X-ray nanofocusing, *AIP conference proceedings* 1764, 020001, 2016.
- [30] A. Last, PhD-thesis: Fehllicht in LIGA-Mikrospektrometern, Universität Karlsruhe, 2003.
- [31] M. Simon, E. Reznikova, V. Nazmov, A. Last and W. Jark, X-ray prism lenses with large apertures, *Proc. SPIE* 7077, 70771Q, 2008.
- [32] F. Koch, F. Marschall, J. Meiser, O. Márkus, A. Faisal, T. Schröter, P. Meyer, D. Kunka, A. Last and J. Mohr, Increasing the Aperture of X-ray Mosaic Lenses by Freeze Drying, *Journal of Micromech. Microeng.* 25, 075015, 2015.
- [33] O. Márkus and F. Koch, Photoresiststruktur und Verfahren zu ihrer Herstellung, Patent DE102015217201B3, 2017.

-
- [34] Chr. G. Schroer, F.-E. Brack, R. Brendler, S. Hönig, R. Hoppe, J. Patommel, St. Ritter, M. Scholz, A. Schropp, F. Seiboth, D. Nilsson, J. Rahomäki, F. Uhlén, U. Vogt, J. Reinhardt and G. Falkenberg, Hard X-Ray Nanofocusing with Refractive X-Ray Optics: Full Beam Characterization by Ptychographic Imaging, Proc SPIE 8848, Advances in X-Ray/EUV Optics and Components VIII; 884807, 2013.
- [35] VDI/VDE 5575 sheet 1, X-ray optical systems - Terms and definitions, Berlin, Beuth Verlag, 2018.
- [36] C. Jacobsen, X-ray microscopy, Advances in microscopy and microanalysis, Cambridge University Press, 2020.
- [37] F. Marschall, PhD-thesis: Entwicklung eines Röntgenmikroskops für Photonenenergien von 15 keV bis 30 keV, Karlsruhe Institute of Technology, KIT Scientific Publishing, 2014.
- [38] St. G. Lipson, H. Lipson and D. St. Tannhauser, Optical Physics, United Kingdom: Cambridge, p. 340, 1998.
- [39] F. Marschall, A. Last, M. Simon, M. Kluge, V. Nazmov, H. Vogt, M. Ogurreck, I. Greving and J. Mohr, X-ray Full Field Microscopy at 30 keV, Journal of Physics: Conference Series (JPCS) 499, 012007, 2014.
- [40] M. A. Kumakhov and V. A. Sharov, A neutron lens, Nature vol. 357, p. 390-391, 1992.
- [41] J. H. Kinney, Q. C. Johnson, U. Bonse, M. C. Nichols, R. A. Saroyan, R. Nusshardt, R. Pahl, J. M. Brase, Three Dimensional X-Ray Computed Tomography in Materials Science, MRS bulletin, Vol.13 (1), p. 13-18, 1988.
- [42] P. C. Johns and M. J. Yaffe, X-ray characterisation of normal and neoplastic breast tissues, Phys. Med. Biol. 32 (6), p. 675-695, 1987.

- [43] I. Manke, Ch. Hartnig, M. Grünerbel, W. Lehnert, N. Kardjilov, A. Haibel, A. Hilger, and J. Banhart and H. Riesemeier, Investigation of water evolution and transport in fuel cells with high resolution synchrotron x-ray radiography, *Appl. Phys. Lett.* 90, 174105, 2007.
- [44] L. Salvo, P. Cloetens, E. Marie, S. Zabler, J. J. Blandine, J. Y. Buffière, W. Ludwig, E. Boller, D. Bellet and C. Josserond, X-ray micro-tomography an attractive characterisation technique in materials science, *Nucl. Inst. & Meth. Sect. B* 200, p. 273–286, 2003.
- [45] J. Baruchel, J. Y. Buffiere and E. Maire, X-ray tomography in material science, Hermes science publications, 2000.
- [46] U. Bonse, F. Busch, O. Günnewig, F. Beckmann, R. Pahl, G. Delling, M. Hahn and W. Graeff, 3D computed X-ray tomography of human can-cellous bone at 8 microns spatial and 10(-4) energy resolution, *Bone Miner.* 1, p. 25-38, 1994.
- [47] A. Blanke, B. Wipfler, H. Letsch, M. Koch, F. Beckmann, R. Beutel and B. Misof, Revival of Palaeoptera-head characters support a monophyletic origin of Odonata and Ephemeroptera (Insecta), *Cladistics* 28 (6), p. 560-581, 2012.
- [48] K.-J. Kim, Brightness, coherence and propagation characteristics of synchrotron radiation, *Nucl. Instr. and Meth.* A246, p. 71-76, 1986.
- [49] N. A. Vinokurov, O. A. Shevchenko and V. G. Tcheskidov, Variable-period permanent magnet undulators, *Phys. Rev. ST Accel. Beams* 14, 040701, 2011.
- [50] J. Hsieh, *Computed tomography: Principles, design, artefacts, and recent advances*, SPIE and John Wiley & Sons Inc., 2nd edition, 2009.
- [51] M. Engelhardt, High-resolution differential phase contrast imaging using a magnifying projection geometry with a microfocus X-ray source, *Appl. Phys. Lett.* 90, 224101, 2007.

-
- [52] A. Snigirev, V. Kohn, I. Snigireva, and B. Lengeler, A compound refractive lens for focusing high energy X-rays, *Nature* 384, p. 49-51, 1996.
- [53] B. Lengeler, C. G. Schroer, B. Benner, A. Gerhardus, T. F. Günzler, M. Kuhlmann, J. Meyer and C. Zimprich, Parabolic refractive X-ray lenses, *Journal of Synchrotron Radiation* 9, p. 119-124, 2002.
- [54] M. A. Fresnel, *Mémoire sur un nouveau système d'éclairage des phares*, Imprimerie royale, Paris, 1822.
- [55] I. Greving, F. Wilde, M. Storm, J. Herzen, J. Hammel, A. Hipp, F. Friedrich, L. Lottermoser, Th. Dose, H. Burmester, M. Müller and F. Beckmann, P05 imaging beamline at PETRA III: first results, *Proc. of SPIE* 9212, 92120O-8, 2014.
- [56] F. Wilde, M. Ogurreck, I. Greving, J. U. Hammel, F. Beckmann, A. Hipp, L. Lottermoser, I. Khokhriakov, P. Lytaev, Th. Dose, H. Burmester, M. Müller and A. Schreyer, Micro-CT at the imaging beamline P05 at PETRA III, *AIP Conference Proceedings* 1741, 030035, 2016.